

1 **Title:**

2 *Impacts of Greenland Block Location on Clouds and Surface Energy Fluxes over the Greenland*

3 *Ice Sheet*

4

5 **Authors:**

6 Jamie L. Ward¹, Mark G. Flanner¹, Etienne Dunn-Sigouin²

7

8 ¹Department of Climate and Space Sciences and Engineering, University of Michigan, Ann
9 Arbor, Michigan, USA.

10 ²Geophysical Institute, University of Bergen and Bjerknes Center for Climate Research, Bergen,
11 Norway

12

13

14 Corresponding Author: Jamie L. Ward – Climate and Space Research Building 2455 Hayward,

15 Ann Arbor, MI 48109

16

This is the author manuscript accepted for publication and has undergone full peer review but has not been through the copyediting, typesetting, pagination and proofreading process, which may lead to differences between this version and the [Version of Record](#). Please cite this article as doi: [10.1029/2020JD033172](https://doi.org/10.1029/2020JD033172)

17 **Abstract:**

18 Clouds and blocking activity have been implicated as causes of increased Greenland Ice
19 Sheet (GrIS) melt in the twenty-first century. Although Greenland blocks (i.e., long-lasting,
20 mostly stationary anticyclones) generally reduce cloud cover and move warm air over
21 Greenland, the elevated GrIS perturbs air and moisture transport in complex ways, implying a
22 need to better understand how blocks affect cloud and surface energy flux anomaly patterns. In
23 this study, we use a combination of daily MODIS cloud data and meteorological and energy flux
24 data from MERRA-2 reanalysis to better understand how Greenland block location, separated
25 into four equal-area quadrants, affects regional cloud and surface energy flux spatial patterns in
26 the summer months of 2002-2018. Overall, cloud fraction and cloud water path reductions are
27 approximately four times greater during northern block days than southern block days. Net cloud
28 radiative forcing anomalies are negative for all Greenland block locations because negative
29 longwave cloud radiative forcing anomalies exceed positive shortwave cloud radiative forcing
30 changes. However, greater cloud cover reductions during northern block days produce more
31 negative net cloud radiative forcing anomalies than southern block days. Greenland-average (i.e.,
32 latitude-weighted average of all GrIS grids) net surface energy flux anomalies range from
33 $+7 W/m^2$ to $+12 W/m^2$ for all block quadrants. While net shortwave energy anomalies
34 dominate the total surface energy response during western Greenland block days, sensible
35 heating is responsible for approximately half of positive total surface energy change during
36 eastern Greenland block days.

37

38 **Key Points:**

39 • Greenland-wide cloud reduction produced by northern block days is at least four times
40 greater than southern Greenland block days.

41 • Block-based cloud reductions produce negative Greenland-wide total cloud radiative
42 forcing changes for all Greenland block quadrants.

43 • Total surface energy blocking changes are influenced more by radiative (non-radiative)
44 fluxes during western (eastern) Greenland block days.

45

46 **1. Introduction**

47 Many atmospheric processes affect Greenland Ice Sheet (GrIS) surface energy fluxes and
48 subsequent surface mass balance changes. Clouds impact the GrIS surface by reflecting
49 insolation away from the surface (i.e., cooling) while also trapping and reemitting longwave
50 energy (i.e., warming). Over snow-covered surfaces like the GrIS, the magnitude of this cloud
51 radiative forcing is affected by cloud properties like ice-to-liquid cloud content ratios, cloud
52 height, and cloud water path (i.e., Shupe and Intrieri, 2004). Liquid-bearing clouds, which are
53 most common over Greenland during the summer months (Shupe et al., 2013; Miller et al., 2015;
54 Van Tricht et al., 2016; Lenaerts et al., 2017), enhance net radiative surface energy flux by
55 largely increasing longwave energy fluxes and only marginally dimming surface insolation
56 (Shupe and Intrieri, 2004; McIllhatan et al., 2017). Optically-thin, low-lying liquid-bearing
57 clouds are optimal for increasing surface radiative energy flux (Bennartz et al., 2013; Van Tricht
58 et al., 2016). In recent years and in future climate projections, liquid-bearing clouds contribute to
59 melt over much of the GrIS (Bennartz et al., 2013; Van Tricht et al., 2016; Hofer et al., 2019).

60 One factor that increases Greenland cloud fraction is enhanced atmospheric water vapor
61 from local- and remotely sourced moisture transport (Johansson et al., 2017; Ballinger et al.,
62 2019). Although summertime moisture amounts and source regions vary regionally over
63 Greenland (e.g., Nusbaumer et al., 2019), a large portion of atmospheric water vapor originates
64 over the North Atlantic. This warmer, moister air moves over the GrIS surface and can influence
65 not only clouds but also skin surface temperatures and snowmelt rate (Pfahl et al., 2015;
66 Mattingly et al., 2018). Over the last 20 years, available water vapor over Greenland has
67 increased with warming air temperatures (Mattingly et al., 2016) and will likely affect
68 Greenland's future climate through surface melt feedbacks related to increased cloud cover.

69 Atmospheric dynamics affect GrIS surface processes by influencing cloud formation,
70 moisture transport, and temperature advection. These processes are complicated by airflow
71 changes that result because of the elevated GrIS surface. Greenland “blocks” (i.e., quasi-
72 stationary anticyclones lasting for days-to-weeks) increase GrIS melt through warm air advection
73 and cloud suppression (Box et al., 2012; Fettweis et al., 2013; Hanna et al., 2014; McLeod and
74 Mote, 2016; Hofer et al., 2017; Mattingly et al., 2018). The resulting cloud reduction and warm
75 air advection from blocking enhance insolation and sensible heat fluxes, respectively, which can
76 enhance surface melt (Hanna et al., 2014; Rajewicz and Marshall, 2014; Lim et al., 2016;
77 Mioduszewski et al., 2016; Hofer et al., 2017). In addition, Greenland blocking is likely related
78 to regional atmospheric moisture transport processes (i.e., Mattingly et al., 2018; Nusbaumer et
79 al., 2019), and thus also cloud patterns and phase. Over Summit, liquid-bearing clouds have
80 larger cloud water paths and are longer-lived during block-like (i.e., ridging) flow regimes
81 (Edwards-Opperman et al., 2018). Summertime Greenland blocking activity has significantly
82 increased over the past twenty years (i.e., Fettweis et al., 2013; Rajewicz and Marshall, 2014;
83 Belleflamme et al., 2015; Hanna et al., 2016; McLeod and Mote, 2016; Hanna et al., 2018) and is
84 another potential contributor to GrIS snowmelt enhancement (Rignot et al., 2008; Fettweis et al.,
85 2011; Shepherd et al., 2012; Tedesco and Fettweis, 2020).

86 The surface mass balance and energy flux effects resulting from different wind patterns
87 and cloud locations vary spatially over the GrIS. Compared to eastern Greenland,
88 westerly/southerly winds produce more cloud cover over western Greenland in the summer
89 months that significantly reduces insolation while enhancing longwave fluxes and surface melt
90 (Cawkwell and Bamber, 2002; Cullather et al., 2018). Moisture transport over western Greenland
91 also has a larger impact on local GrIS snowmelt because the air is warmer and moister than over

92 eastern Greenland (Mattingly et al., 2018). The effects of Greenland blocking on cloud cover
93 (e.g., Lim et al., 2016; Hofer et al., 2017), temperature advection, and subsequent snowmelt and
94 surface energy flux processes (e.g., Fettweis et al., 2013; Belleflamme et al., 2015; Tedesco et
95 al., 2016; Noël et al., 2019) also exhibit spatial variability and have been explored in previous
96 studies. However, these studies investigate average blocking conditions that do not account for
97 the quasi-stationary nature of Greenland blocks (e.g., Chen and Luo, 2017). Different block
98 locations could produce variations in cloud, moisture transport, and surface energy flux patterns
99 by changing air source regions and how block airflow interacts with the GrIS surface, which
100 could directly impact GrIS surface mass balance processes.

101 In this study, we use a combination of reanalysis and satellite cloud data to document and
102 differentiate the effects of summertime (i.e., June through August) Greenland block location on
103 cloud formation, moisture transport, and surface energy flux processes over the GrIS. First, we
104 describe the datasets, blocking detection algorithm, and statistical methods we use for this study.
105 Next, we explore the impacts of block location on cloudiness in terms of moisture transport,
106 temperature, and airflow patterns. We then explore the implications of cloud changes on
107 Greenland-wide cloud radiative forcing and total surface energy fluxes.

108

109 **2. Methods**

110 2.1) Greenland Block Data and Detection

111 We use Modern-Era Retrospective Analysis for Research and Applications, version 2
112 (MERRA-2) reanalysis data to find blocks and analyze their associated meteorological and
113 surface energy flux patterns over the GrIS (Gelaro et al., 2017). Daily averages are calculated
114 from all sub-daily MERRA-2 meteorological and surface energy flux fields. Because we are

115 interested in blocking-induced cloud and surface energy flux anomalies that could materially
116 impact summer surface melt, we analyze blocks in June, July, and August (JJA) from 2002
117 through 2018. We include days in late May and early September if they are part of early June
118 and late August blocking events, respectively.

119 To detect blocks in the MERRA-2 dataset, we use a modified version of the Dunn-
120 Sigouin et al. (2013) algorithm (hereafter referred to as D-S) (see Table 1). The multi-step
121 approach of the D-S algorithm requires the satisfaction of multiple conditions to classify events
122 as blocks (Dunn-Sigouin et al., 2013). In brief, the D-S method tracks contiguous groupings of
123 500hPa geopotential height anomalies (Z'_{500}) meeting minimum pre-established amplitude
124 threshold (A) and area requirements (S) over time. For each latitude/longitude grid, we calculate
125 Z'_{500} between May 16 and September 15 with the following formula:

$$126 \quad Z'_{500}(n) = Z_{500}(n) - Z_{clim}(n) \quad (1),$$

127 where $Z_{clim}(n)$ is the climatological average 500hPa geopotential height at each grid point.
128 Z_{clim} is defined using a Gaussian-weighted, 31-day moving window centered on day n for all 17
129 years (2002-2018) of 500hPa geopotential height data. Gaussian weighting places more emphasis
130 on days close to n , incorporating seasonal variability in Z_{500} . In the D-S algorithm, a block is
131 recorded if 1) the Z'_{500} areas between consecutive days overlap (O) by a certain percentage, and
132 2) these anomalies exist for a predefined number of days (D). Although the original D-S
133 detection algorithm further tests for a Z_{500} gradient reversal equatorward of the block, we do not
134 maintain this requirement because persistent high pressure ridging is a prominent variety of
135 blocking in the Greenland region (Fettweis et al., 2013; Hanna et al., 2014; Tedesco et al., 2016).
136 Notably, we define blocks using a duration of 4 days in the algorithm to detect the July 2012
137 blocking event (e.g., Tedesco et al., 2013). With this change, the July 2012 block lasts for 7 days

138 (i.e., Table S3), so we only include blocks lasting at least 5 days in the remainder of our analysis
139 in agreement with previous blocking research (e.g., Häkkinen et al., 2014; McLeod and Mote,
140 2016). Greenland block detection is sensitive to algorithm structure and threshold values within
141 the algorithm (e.g., Woollings et al., 2018). We use this specific set of parameters because they
142 identify a large number of events while also identifying events that are strong enough to impact
143 the Greenland surface energy budget, like the July 2012 blocking event (e.g., Tedesco et al.,
144 2013). More details about the D-S algorithm can be found in Dunn-Sigouin et al. (2013).

145 The block location for each block day detected in the modified D-S setup is determined
146 using the equal-area block quadrants defined in Fig. 1A (latitude and longitude boundaries for
147 each quadrant are provided in the supplementary information section, Table S1). Within the
148 contiguous area of highlighted Z'_{500} grids closest to/over Greenland for each block day, we find
149 the local maximum Z'_{500} latitude/longitude coordinate. We then find its corresponding Z_{500}
150 maximum latitude/longitude grid point and bin it in one of the four Greenland block quadrants
151 (Fig. 1A). We look for maximum coordinates in both Z'_{500} and Z_{500} because regions of high
152 geopotential height anomalies may not entirely cover the 500hPa block area. Because
153 midlatitude ridging can result in Z_{500} center points south of our Greenland domain, we allow
154 Z_{500} to lie marginally outside of the defined block quadrants.

155

156 2.2) Greenland Cloud Data

157 We use Moderate Resolution Imaging Spectroradiometer (MODIS) Terra Collection 6,
158 Level 2 cloud data (product code MOD06), which extends from 2002 to present (Platnick et al.,
159 2017), to analyze cloud conditions during Greenland blocking. We choose MOD06 data because
160 of its high spatial and temporal coverage, as well as its incorporation of processing algorithm

161 improvements for high latitude opaque cloud detection and characterization over the reflective
162 GrIS snow (Ackerman et al., 1998; Liu et al., 2010; Platnick et al., 2017). The cloud water path
163 and cloud optical thickness fields we use are produced by the combination of 1.6 μ m and 2.1 μ m
164 bands for better surface-cloud differentiation (Platnick et al., 2001). Although MOD06 data are
165 accompanied by detection uncertainties, we do not include these here.

166 To better compare the MERRA-2 data to the corresponding daily cloud conditions, we
167 spatially aggregate 1x1km and 5x5km along-swath gridded granule MOD06 data onto the 0.5° ×
168 0.625° MERRA-2 grid and average all resulting cloud data for each day. This regridded, daily-
169 averaged MOD06 data covers 60 – 85°N latitude and 93.125°W – 13.125°E longitude to
170 accommodate clouds corresponding to blocking in each block quadrant. We first aggregate
171 1x1km fields onto the 5x5km grid for each MODIS granule. Because cloud water path
172 observations are only collected during the day, we exclude “nighttime” pixels with solar zenith
173 angle values exceeding 81.36° degrees for all other cloud variables (Platnick et al., 2017). We
174 then aggregate 5x5km granule data onto the larger MERRA-2 grid by averaging the closest
175 5x5km data points onto each MERRA-2 grid point. Apart from cloud fraction and cloud phase,
176 all MOD06 variables are averaged onto the MERRA-2 grid with cloud fraction weighting for
177 each MODIS granule. Finally, we average (using cloud fraction weighting) each MERRA-2
178 gridded MOD06 data field over time to create daily average cloud fields.

180 2.3) Meteorological and Cloud Radiative Forcing Calculations

181 Because cloud formation depends on the presence of atmospheric moisture, we evaluate
182 moisture transport ($kg\ m^{-1}\ s^{-1}$) during blocking in each block quadrant, during all blocks
183 combined, and during non-block days (i.e., JJA 2002-2018 days that do not exhibit blocking) to

184 gain a first-order understanding of the effects of blocking on clouds and surface processes.

185 Similar to Woods et al. (2013), we calculate daily gridded total column moisture transport as:

$$186 \quad F = \frac{1}{g} \int_{400}^{p_s} Q(p) * W(p) dp \quad (2).$$

187 In (2), F is the resulting total column moisture flux, g is the acceleration of gravity ($9.8 m/s^2$),

188 $Q(p)$ is specific humidity at pressure level p , $W(p)$ is the wind velocity at p , and p ranges from

189 pressure at the surface (p_s) to 400hPa (Woods et al., 2013). We calculate $W(p)$ speed and

190 direction at each grid point using zonal and meridional wind vectors at the corresponding

191 pressure level. Total column wind vectors (\vec{W}) are calculated from pressure-weighted, column-

192 integrated zonal and meridional winds over all pressure levels. Because of GrIS surface elevation

193 variability and daily changes in atmospheric pressure, p_s is spatially and temporally variable in

194 our Greenland domain.

195 GrIS surface energy balance is important to disentangle the effects of block location and

196 subsequent cloud processes on snowmelt. We calculate total surface energy flux as the sum of

197 net shortwave energy, net longwave energy, sensible heat flux, and latent heat flux at each point

198 in the Greenland domain (e.g., van den Broeke et al., 2017; Lenaerts et al., 2019). We do not

199 include conductive heat flux in our surface energy balance calculation because its magnitude is

200 negligible in ice covered regions (Yang et al., 2011). In addition, to examine the impacts of

201 clouds in each blocking case on net surface radiative fluxes, we calculate total surface cloud

202 radiative forcing using all-sky (all) and clear-sky (clr) quantities:

$$203 \quad CRF_{TOTAL} = CRF_{SW} + CRF_{LW} = (SW_{net,all} - SW_{net,clr}) + (LW_{net,all} - LW_{net,clr}) \quad (3).$$

204 Because high-latitude insolation varies strongly with time of year, our subsets of regional block

205 and non-block days are subject to different mean insolation. To account for this, we use

206 MERRA-2 downwelling top-of-atmosphere shortwave energy data to scale surface shortwave

207 flux-related fields so they represent consistent “summer-mean” values. We calculate separate
208 GrIS-wide top-of-atmosphere incoming solar radiation averages for summer (i.e., all days in
209 JJA), “Control” (i.e., JJA non-block days), and block days belonging to each block quadrant (i.e.,
210 “All Blocks”, NW, NE, SW, and SE). We divide this summer average by the corresponding
211 “Control” and block day mean insolation to calculate shortwave scaling factors that are used to
212 normalize our filtered surface and cloud shortwave fluxes. These scaling factors are listed in
213 Table S2. Surface energy flux components are considered to be positive in the downward
214 direction because they positively contribute to total surface energy.

215 We differentiate surface energy fluxes, meteorological conditions, and cloud properties
216 between block days in each quadrant, “All Blocks”, and non-block days (“Control”) using two-
217 sample t-testing for each coordinate and spatial averaging over the GrIS. In the case of spatial
218 averages, we define GrIS pixels as those having at least 50% land ice coverage, as defined with
219 the MERRA-2 land ice surface fractions.

220

221 **3. Results and Discussion**

222 3.1) Blocking Statistics

223 Here, we briefly describe the frequency characteristics of block days belonging to
224 persistent blocking activity (i.e., blocks lasting at least 5 days from D-S output) for “All Blocks”
225 and individual block quadrants. We find a total of 205 summer block days associated with 30
226 blocking events. Four of these blocking events extend outside of JJA (see Table S3 for block day
227 list). There are ~12.1 block days per summer, on average, with a standard deviation of ~10.5
228 days. This year-to-year variability in block day count results from varying synoptic- to planetary-
229 scale dynamics. We find above-average summer block day counts in 2003, 2006-2008, 2012, and

230 2015- 2016 (Fig. S1), which aligns well with previously reported Greenland blocking
231 frequencies (e.g., Fettweis et al., 2011; Fettweis et al., 2013; Hanna et al., 2016; Tedesco et al.,
232 2016).

233 Binning block days to our defined block quadrants (i.e., Fig. 1A) provides us with
234 additional information about preferred blocking regions around Greenland. From Fig. 2A, and in
235 agreement with previous studies (i.e., Häkkinen et al., 2014; McLeod and Mote, 2015;
236 Cullather et al., 2018), the average “All Blocks” block center is located over south-central
237 Greenland. NW and NE blocks are smaller but maintain similar geopotential heights to SW and
238 SE blocks. Overall, we find that the southwest (SW) and southeast (SE) block quadrants contain
239 more block days (69 and 80 days, respectively) than the northwest (NW) and northeast (NE)
240 block quadrants (35 and 21 days, respectively). However, northern quadrant block days
241 constitute 27% of all detected Greenland block days during 2002-2018 and are thus important to
242 Greenland’s climate.

244 3.2) Clouds and Block Location

245 In this section, we explore MOD06 cloud fraction (Fig. 3) and cloud water path changes
246 (Fig. S2) over the Greenland Ice Sheet for “All Blocks” and individual block quadrants with
247 respect to “Control”. We use moisture transport and wind fields (Fig. 4) to explain the resulting
248 cloud anomaly patterns for each blocking case. Liquid cloud fraction, ice cloud fraction, cloud
249 top height, cloud top temperature, and cloud optical thickness are all included in the
250 supplementary information.

251 We can see in Fig. 3 that cloud fraction anomaly distributions are different between “All
252 Blocks” and individual block quadrants. Regardless of block location, however, composite

253 500hPa geopotential height block centers (Fig. 2) are collocated with negative cloud fraction
254 anomalies because of high pressure subsidence (Box et al., 2012; Hanna et al., 2014; Rajewicz
255 and Marshall, 2014; Lim et al., 2016; Mioduszewski et al., 2016; Hofer et al., 2017). In the case
256 of “All Blocks”, cloud fraction anomalies are negative over most of the GrIS (Fig. 3C). The most
257 negative of these cloud fraction changes is located over southern Greenland and coincides with
258 the average “All Blocks” high pressure center (Fig. 2A). In agreement with previous studies
259 (e.g., Hofer et al., 2017; Delhasse et al., 2018), limited positive cloud fraction anomalies in
260 north-central Greenland result from onshore, westerly airflow (Fig. 4A) that cools adiabatically
261 and condenses. Overall, Greenland-average (i.e., latitude-weighted average of all GrIS grids)
262 cloud fraction decreases by 0.04 in “All Blocks”.

263 Outside of the block centers for each block location, we find that NW and NE block day
264 cloud fraction change patterns are markedly different from those for SW and SE block days. In
265 these cases, easterly winds flow (Fig. 4C-4D) downslope from central Greenland and warm
266 adiabatically to inhibit cloud formation. NW block days also produce significant cloud fraction
267 enhancements over the eastern half of the GrIS (Fig. 3D) because of rising northerly airflow
268 (Fig. 4C). Despite these small regions of increased cloudiness, Greenland-average cloud fraction
269 is reduced by 0.09 and 0.12 during NW and NE block days, respectively (Fig. 3D-3E). Cloud
270 fraction anomaly spatial patterns reverse for SW and SE block days. Namely, SW and SE
271 blocking produce enhanced cloud fractions over portions of western Greenland and cloud
272 fraction reductions over eastern Greenland. Cloud fraction changes for southern Greenland block
273 days more closely represent “All Blocks” cloud fraction changes because they constitute a
274 majority of all block days. Positive cloud fraction anomalies over northern Greenland are
275 produced by westerly-based winds moving upslope over the GrIS margins (Fig. 4E-4F) that

276 adiabatically enhance cloud cover (i.e., Neff et al., 2014; McLeod and Mote, 2015;
277 Mioduszewski et al., 2016; Mattingly et al., 2018). SE block days reduce cloud fractions along
278 the eastern GrIS margins because westerly airflow adiabatically warms as it descends from the
279 central GrIS towards the eastern shoreline. Similarly for SW block days, we calculate reduced
280 cloud coverage over southeastern Greenland because of downslope airflow. Despite more
281 prevalent cloud fraction enhancement over the GrIS during SE block days, GrIS-average cloud
282 fraction anomalies are still negative (-0.02).

283 Cloud water path anomaly patterns (Fig. S2) for each blocking case are similar to cloud
284 fraction changes; areas of reduced cloud fraction align with areas of decreased cloud water path,
285 and vice versa. Negative cloud water path changes occur for all block locations despite greater
286 moisture availability relative to “Control” (Table S4) because of subsidence-produced
287 atmospheric stability. However, cloud water path anomalies are more negative for NW and NE
288 block days because their available moisture is sourced from the cold, dry Arctic Ocean and
289 Greenland Sea, respectively (Nusbaumer et al., 2019). In contrast, SW and SE block day
290 moisture is sourced from the warmer North Atlantic Ocean (e.g., Neff et al., 2014; McLeod and
291 Mote, 2015; Mioduszewski et al., 2016; Mattingly et al., 2018). Cloud water path reductions can
292 reduce cloud shortwave scattering (Bennartz et al., 2013) and influence surface cloud radiative
293 forcing.

294 From these results, we can see that cloud anomaly patterns differ by block location,
295 especially between northern quadrant and southern quadrant block days. NW and NE blocking
296 produce greater cloud fraction and cloud water path reductions relative to “Control”, especially
297 over western Greenland. In contrast, SW and SE block days enhance (reduce) cloud fraction and
298 cloud water paths over portions of western (eastern) Greenland. These differences arise from 1)

299 persistent, anticyclonic airflow over Greenland's elevated surface and 2) moisture prevalence
300 and source region. As we will see in the following section, cloud properties for different block
301 locations can directly affect energy fluxes received at the surface.

302

303 3.3) Cloud Radiative Forcing and Block Location

304 In the previous section, we found that NW and NE quadrant blocking produce greater
305 GrIS-wide cloud fraction and cloud water path reductions than SW and SE block days. We
306 combine our cloud results with MERRA-2 shortwave and longwave cloud radiative forcing data
307 to investigate the impacts of block location on surface radiative energy. To disentangle the
308 effects of clouds on radiative fluxes, we use clear-sky and all-sky shortwave and longwave
309 fluxes to calculate cloud radiative forcing (equation 3). Although cloud radiative forcing does not
310 account for net surface energy changes, it is a useful metric for explaining radiative impacts of
311 the actual clouds (Intrieri et al., 2002; Wang et al., 2019). All energy fluxes are defined as
312 positive in the downward direction (i.e., into the surface).

313 Clouds in "All Blocks" and "Control" days produce negative absolute shortwave cloud
314 radiative forcing because of scattering (Fig. 5A-5B). However, because cloud fraction and cloud
315 water path reductions in "All Blocks" reduce scattering above the surface, positive shortwave
316 cloud radiative flux anomalies result over most of the GrIS (Fig. 5C). Similarly, we find positive
317 (negative) shortwave cloud radiative forcing anomalies for negative (positive) cloud fraction
318 changes in each of the block quadrant cases (Fig. 5D-5G). NW and NE block days display
319 significant shortwave cloud radiative forcing enhancements over western Greenland and within
320 their respective block quadrant boundaries, while SW and SE block days exhibit positive
321 shortwave cloud radiative forcing changes over portions of eastern Greenland. Overall, spatially-

322 averaged shortwave cloud radiative forcing anomalies are largest during NW and NE block days
323 ($+3.63 W/m^2$ and $+4.71 W/m^2$ respectively; Fig. 5D, 5E).

324 We see the changes of the opposite sign in longwave surface cloud radiative forcing
325 during blocking (Fig. 6). “All Blocks” longwave cloud radiative forcing anomalies are
326 significantly negative over most of the GrIS (Fig. 6C). Similarly, blocking in each block
327 quadrant produces negative longwave cloud radiative forcing anomalies in regions of reduced
328 cloudiness. Despite positive atmosphere temperature anomalies during blocking (i.e., Fig. S3),
329 reduced cloud cover decreases downwelling longwave energy (i.e., Shupe and Intrieri, 2004;
330 Miller et al., 2015) while surface-based upwelling longwave energy remain approximately
331 constant (not shown), which produces negative changes in net longwave cloud radiative forcing
332 (van As et al., 2012; Lenaerts et al., 2019). Like our shortwave cloud radiative forcing results, we
333 find NW and NE blocking produce Greenland-average longwave cloud radiative forcing
334 reductions ($-8.37 W/m^2$ and $-9.65 W/m^2$) that are 2-3 times greater than those for SW and
335 SE block days because of larger cloud fraction and cloud water path reductions.

336 When we compute net cloud radiative forcing anomalies for each blocking case (Fig. 7),
337 we find that longwave cloud radiative forcing anomalies outweigh shortwave cloud radiative
338 forcing anomalies and result in dominantly negative net cloud radiative forcing. These net cloud
339 radiative forcing anomaly patterns resemble cloud fraction and cloud water path changes during
340 all blocking scenarios. Larger longwave cloud radiative forcing contributions to net cloud
341 radiative forcing anomalies aligns with previous studies on Greenland cloud radiative forcing
342 (Miller et al., 2015; Van Tricht et al., 2016). NW and NE blocks produce the most negative net
343 cloud radiative forcing changes ($-4.75 W/m^2$ and $-4.94 W/m^2$, respectively) that have

344 magnitudes approximately 2 times larger than net cloud radiative forcing anomalies for SW and
345 SE block days ($-2.45 W/m^2$ and $-1.23 W/m^2$).

346 NW and NE block days exhibit larger positive shortwave cloud radiative forcing
347 anomalies and more negative longwave cloud radiative forcing anomalies than southern quadrant
348 blocking because of greater cloud cover reductions. In the case of shortwave cloud radiative
349 forcing changes, we hypothesize that positive ice cloud fraction (Fig. S5) and negative liquid
350 cloud fraction (Fig. S4) changes during NE and SE block days also increase net shortwave cloud
351 radiative forcing (compared to NW and SW block days, respectively) by reducing cloud albedo.
352 For each block location, however, longwave cloud radiative forcing changes outweigh shortwave
353 cloud radiative forcing changes, resulting in negative cloud radiative effects over the GrIS
354 because of reduced cloudiness. These findings demonstrate that block location is important not
355 only for cloud changes over Greenland but also for associated cloud radiative forcing anomalies.

356

357 3.4) Surface Energy Fluxes and Block Location

358 Because changes in net surface energy fluxes are impacted by factors other than cloud
359 presence (e.g., air temperature, moisture availability, and surface albedo), we calculate net
360 surface shortwave and longwave flux anomalies for each block location. Overall, Greenland-
361 average net radiative flux (i.e., the sum of net shortwave and net longwave fluxes) increases for
362 all blocking cases (Figs. S9 and S10). Net shortwave flux anomalies are especially large over the
363 GrIS margins (Fig. S9) because of corresponding albedo reduction. Unlike southern quadrant
364 block days, negative net longwave flux anomalies produced by northern quadrant blocking
365 partially offset positive changes in net shortwave fluxes. SW and SE blocking leads to positive
366 surface shortwave and longwave flux anomalies (SW block day net longwave responses are

367 minimal) because of smaller cloud fraction reductions and moisture transport processes (Fig.
368 S10). These positive net radiative flux anomalies correspond to negative Greenland-average total
369 cloud radiative forcing, which highlights the importance of other phenomena apart from clouds
370 for impacting surface radiative fluxes.

371 Sensible and latent heat fluxes are also important for total surface energy input during
372 blocking. As we can see from Fig. 8, significant sensible heat flux anomalies are dominantly
373 positive for all block locations. However, NE and SE block days show larger Greenland-wide
374 sensible heat anomalies ($+8.98 \text{ W/m}^2$ and $+5.49 \text{ W/m}^2$, respectively) than NW and SW block
375 days. Since warm air advection and adiabatic warming of descending airflow have both been
376 shown to contribute to greater downward-directed sensible heat flux (e.g., Box et al., 2012;
377 Fausto et al., 2016; Välisuo et al., 2018), we examine 2m-temperature anomalies and wind
378 patterns for these cases. All block locations exhibit significantly positive 2m-temperature
379 anomalies (Fig. S3), but the combination of downslope and southerly airflow patterns (Fig. 4)
380 onto northern(western) Greenland enhance local warming and produce larger sensible heat flux
381 anomalies during NE(SE) block days. NW and SW blocking, on the other hand, produce
382 northerly and westerly winds that flow upslope toward the central GrIS (Fig. 4). These winds
383 cool adiabatically and lead to smaller sensible heat anomalies. Although latent heat flux
384 anomalies are non-negligible, they are small in comparison with radiative and sensible heat
385 fluxes, so we do not include these findings here (see supplementary information Fig. S11).

386 Now that we have examined cloud radiative forcing, radiative fluxes, and turbulent heat
387 fluxes associated with different Greenland block locations, we will look at the impact of block
388 location on total surface energy flux (E_{total}), defined as the sum of net shortwave, net longwave,
389 sensible, and latent heat fluxes, respectively:

390 $E_{total} = SW_{net} + LW_{net} + SH + LH$ (4).

391 We calculate E_{total} for each grid (Fig. 9), Greenland-wide averages for each block location (Fig.
392 9), and separate GrIS accumulation and ablation zone averages (Fig. 10) to determine how E_{total}
393 changes with elevation. All blocking locations produce large positive surface energy flux
394 changes (Fig. 9) corresponding to GrIS margin albedo reduction (Fig. S9) that exceed
395 accumulation zone net surface energy anomalies (Fig. 10) (e.g., Tedesco et al., 2011). We note
396 that monthly MERRA-2 GrIS surface albedo is consistently smaller than MODIS (i.e., Hall et
397 al., 2018), which could positively bias our net surface energy flux anomaly estimates.

398 Because runoff and snowmelt dominantly occur in the ablation zone, we focus on energy
399 changes for each block location over lower GrIS elevations. We find that total surface energy
400 anomalies are positive for all block locations, with the largest changes being exhibited by NW
401 and NE block days ($+22.33 W/m^2$ and $+22.50 W/m^2$, respectively). Net shortwave anomalies
402 contribute the most to ablation zone net energy changes for all but SE block days
403 ($+11.96 W/m^2$ to $+20.92 W/m^2$), followed by sensible heat flux changes ($+4.50 W/m^2$ to
404 $+9.25 W/m^2$). In contrast, sensible heating ($+6.02 W/m^2$) is the largest contributor to SE
405 block quadrant total surface energy change ($+12.08 W/m^2$). SE block day net longwave energy
406 changes ($+3.25 W/m^2$) to total surface energy change over the ablation zone. NW, NE, and SW
407 block day net longwave flux changes marginally contribute to total surface energy anomalies.

408 Relative contributions of component energy flux anomalies that increase total surface
409 energy vary by block quadrant longitude. Sensible heating contributes more to total surface
410 energy enhancement for NE and SE block days (40-50%) than western quadrant block days (20-
411 30%) because of airflow source region. NE and SE blocking activity circulates warmer air from
412 lower latitudes onto the GrIS ablation zone (Fig. 4) that enhances sensible heat fluxes relative to

413 western block quadrants at the same latitude. Because airflow is derived from cooler regions for
414 NW and SW block days, net shortwave fluxes along the GrIS margins dominate positive surface
415 changes (70-80%). Net shortwave flux anomalies constitute 10-50% of surface energy
416 enhancement for NE and SE block days.

417 Although accumulation zone total surface energy is rarely large enough to trigger melt,
418 surface energy changes can trigger snow aging and reduce surface albedo. We find that, over the
419 GrIS accumulation zone, northerly cold air advection and large cloud reduction result in negative
420 total surface energy anomalies for NW block days ($-0.62 W/m^2$). All other block locations
421 produce smaller positive total surface energy changes over higher elevations ($+6.04 W/m^2$ to
422 $+8.39 W/m^2$; Fig. 10). As a result, NW block days exhibit the lowest Greenland-average net
423 surface flux change ($+7.12 W/m^2$) of all block locations. Out of the remaining blocking
424 locations, NE block days exhibit the largest Greenland-wide net surface energy change
425 ($+12.36 W/m^2$).

426 Greenland block location affects spatial and Greenland-average surface energy fluxes
427 through the production of different cloud patterns, moisture transport and source region, and
428 adiabatic heating resulting from orographic airflow. NW block days are unique from other
429 blocking in other locations because they produce negative net surface energy flux anomalies over
430 the central GrIS and result in the lowest Greenland-average net surface energy flux change.
431 Although we find similar total surface energy flux anomaly patterns between the remaining
432 blocking cases, moisture and airflow changes over the GrIS dictate the relative contribution of
433 turbulent and radiative heat flux anomalies. Sensible heat fluxes contribute more to net surface
434 energy flux changes for NE and SE block days because of enhanced warm air advection and

435 subsidence over southern and western Greenland. Net solar energy anomalies are the largest
436 contributing energy source to net surface energy changes for NW and SW block days.

437

438 **4. Conclusions**

439 In this study, we use a combination of MERRA-2 meteorological reanalysis data and
440 MODIS collection 6, level 2 cloud data to assess the impacts of Greenland block location on
441 regional clouds and Greenland Ice Sheet (GrIS) surface energy fluxes in the summer months of
442 2002-2018. We find block days using a modified setup of the D-S block detection algorithm
443 (Dunn-Sigouin et al., 2013) and separate individual block days using uniquely defined equal-area
444 block quadrants over Greenland. We use moisture transport, winds, and temperature data to
445 explain how block location affects clouds and surface energy fluxes and compare these results on
446 a quadrant-by-quadrant basis.

447 From 2002 through 2018, we find 30 Greenland block events in June, July, and August
448 (JJA), totaling 205 block days. Of these years, the summers of 2003, 2006-2008, 2012, and
449 2015-2016 had higher-than-average block day counts, while our method detects no blocking
450 activity in 2002, 2013, or 2017. Although we verify block activity for each day in our record, we
451 emphasize that block days found by the D-S algorithm (and others) are sensitive to changes in
452 algorithm threshold values. Although most (73%) of these block days are located in the SW and
453 SE block quadrants, understanding cloud and energy flux changes during NW and NE block
454 days (27% of all block days) is also important to fully understanding Greenland blocking.

455 All Greenland block locations produce negative Greenland-average cloud fraction and
456 cloud water path changes, as demonstrated previously (e.g., Lim et al. 2016; Mioduszewski et
457 al., 2016; Hofer et al., 2017; Tedesco and Fettweis, 2020). However, the extent to which cloud

458 coverage and water path decrease, as well as the cloud change patterns over Greenland, vary by
459 block location. Negative cloud fraction and cloud water path anomalies are at least four times
460 greater for NW and NE block days than SW and SE block days because SW and SE quadrant
461 block days import warmer, moister air over the GrIS to damp the extent of cloud reduction
462 caused by block dynamics.

463 Cloud radiative forcing anomalies vary in magnitude and spatial distribution for different
464 block locations. Greenland-average shortwave cloud radiative forcing values are greater for NW
465 and NE block days and correspond to large cloud fraction and cloud water path reductions.
466 However, cloud water path changes in eastern Greenland blocks produce greater shortwave
467 cloud radiative forcing anomalies than western Greenland blocks at the same latitude. Longwave
468 cloud radiative forcing and total cloud radiative forcing anomalies are negative for all block
469 locations, with NW and NE block days producing anomalies at least 2 times as great as SW and
470 SE block day anomalies. Larger longwave cloud radiative forcing anomaly magnitudes indicate
471 that Greenland blocking cloud changes negatively impact the amount of radiative energy
472 absorbed by the surface.

473 Total surface energy flux anomalies over the entire GrIS vary between block quadrants.
474 Over lower elevations, total surface energy changes are lower for SW and SE block days relative
475 to northern quadrant blocking. For all block locations except the SE block quadrant, net
476 shortwave and sensible heat flux changes are the greatest contributors to total surface energy
477 anomalies. SE block day total surface energy increases because of sensible heat and net
478 longwave flux changes. NW block days exhibit the least positive Greenland-average net surface
479 energy change ($+7.12 \text{ W/m}^2$) because of cold air advection and cloud changes over higher
480 elevations. NE blocking produces the greatest Greenland-average net energy flux change

481 (+12.36 W/m^2) because of the combined influence of large positive net shortwave and sensible
482 heat flux anomalies. Although net surface energy flux anomalies are similar for each block
483 location, the component flux anomalies that contribute to these changes are different because of
484 changes in dominant air and moisture source regions.

485 These results all highlight the importance of block location for cloud and surface energy
486 flux patterns over the GrIS. However, some of our chosen methods could affect these findings.
487 One of the most significant constraints in this study is block detection itself. Because there is no
488 concrete definition for blocking, we can justify changes we make to the D-S algorithm
489 thresholds. However, changing these thresholds or using a different detection method to find
490 Greenland blocks from meteorological data could affect the block days identified. Namely,
491 assuming blocks are planetary scale, which is reasonable (e.g., Papritz and Dunn-Sigouin, 2020),
492 the meridional circulation of the block can be linked to vertical motion via the Sverdrup balance
493 (i.e., Wills et al., 2019). Then, stronger blocks will be associated with stronger meridional
494 circulation and vertical cloud motion, yielding potentially greater cloud changes.

495 This study demonstrates that blocks in northern Greenland more effectively reduce cloud
496 cover and decrease total cloud radiative forcing at the surface. Along with clouds, air
497 temperature, moisture, and surface albedo feedbacks also contribute to surface energy changes
498 during blocking, especially for blocking over southern Greenland that draws warm, moist North
499 Atlantic air over the GrIS. Our findings can be used to further understand the impact of block
500 location on GrIS snowmelt processes through the examination of clouds and surface energy
501 fluxes. Importantly, these results indicate that modeled Greenland responses to blocking should
502 also be sensitive to the simulated block location. Biased block locations in model output could

503 complicate our understanding of the modeled impacts of future blocking on GrIS surface
504 processes.

505

506 **Acknowledgements**

507 We acknowledge support from NASA Earth and Space Science Fellowship award

508 80NSSC17K0323. MODIS Collection 6 data can be accessed via

509 <https://ladsweb.modaps.eosdis.nasa.gov/search/> and MERRA-2 data are downloadable from

510 <https://disc.gsfc.nasa.gov/datasets?keywords=MERRA-2&page=1>

511 **References**

512 Ackerman, S.A., Strabala, K.I., Menzel, W.P., Frey, R.A., Moeller, C.C., & Gumley, L.E. (1998,
513 December 27). Discriminating clear sky from clouds with MODIS. *Journal of Geophysical*
514 *Research*, 103(D24), 32,141-32,157.

515

516 Ballinger, T. J., Mote, T. L., Mattingly, K., Bliss, A. C., Hanna, E., van As, D., Prieto, M.,
517 Gharehchahi, S., et al. (2019). Greenland Ice Sheet late-season melt: investigating multiscale
518 drivers of K-transect events, *The Cryosphere*, 13, 2241-2257. [https://doi.org/10.5194/tc-13-2241-](https://doi.org/10.5194/tc-13-2241-2019)
519 [2019](https://doi.org/10.5194/tc-13-2241-2019).

520

521 Belleflamme, A., Fettweis, X., & Erpicum, M. (2015). Recent summer Arctic atmospheric
522 circulation anomalies in a historical perspective. *The Cryosphere*, 9, 53-64, doi:10.5194/tc-9-53-
523 2015.

524

525 Bennartz, R., Shupe, M.D., Turner, D.D., Walden, V.P., Steffen, K., Cox, C.J., et al. (2013, April
526 4). July 2012 Greenland melt extent enhanced by low-level liquid clouds. *Nature*, 496, 83-86,
527 doi:10.1038/nature12002.

528

529 Box, J.E., Fettweis, X., Stroeve, J.C., Tedesco, M., Hall, D.K., & Steffen, K. (2012). Greenland
530 ice sheet albedo feedback: thermodynamics and atmospheric drivers. *The Cryosphere*, 6, 821-
531 839, doi:10.5194/tc-6-821-2012.

532

533 Cawkwell, F.G.L., & Bamber, J.L. (2002). The impact of cloud cover on the net radiation budget
534 for the Greenland ice sheet. *Annals of Glaciology*, *34*, 141-149.

535

536 Chen, X. & Luo, D. (2017). Arctic sea ice decline and continental cold anomalies: Upstream and
537 downstream effects of Greenland blocking, *Geophysical Research Letters*, *44*, 3411-3419,
538 doi:10.1002/2016GL072387.

539

540 Cullather, R.I., & Nowicki, S.M.J. (2018, March 1). Greenland Ice Sheet Surface Melt and Its
541 Relation to Daily Atmospheric Conditions. *Journal of Climate*, *31*, 1897-1919,
542 doi:10.1175/JCLI-D-17-0447.1.

543

544 Delhasse, A., Fettweis, X., Kittel, C., Amory, C., & Agosta, C. (2018). Brief communication:
545 Impact of the recent atmospheric circulation change in summer on the future surface mass
546 balance of the Greenland Ice Sheet. *The Cryosphere*, *12*, 3409-3418. [https://doi.org/10.5194/tc-](https://doi.org/10.5194/tc-12-3409-2018)
547 [12-3409-2018](https://doi.org/10.5194/tc-12-3409-2018).

548

549 Dunn-Sigouin, E., Son, S-W., & Lin, H. (2013, February). Evaluation of Northern Hemisphere
550 Blocking Climatology in the Global Environment Multiscale Model. *Monthly Weather Review*,
551 *141*, 707-727, doi:10.1175/MWR-D-12-00134.1.

552

553 Edwards-Opperman, J., Cavallo, S., & Turner, D. (2018, April). The Occurrence and Properties
554 of Long-Lived Liquid-Bearing Clouds over the Greenland Ice Sheet and Their Relationship to

555 the North Atlantic Oscillation. *Journal of Applied Meteorology and Climatology*, 57, 921-935,
556 doi:10.1175/JAMC-D-17-0230.1.

557

558 Fausto, R.S., van As, D., Box, J.E., Colgan, W., Langen, P.L., & Mottram, R.H. (2016). The
559 implication of nonradiative energy fluxes dominating Greenland ice sheet exceptional ablation
560 area surface melt in 2012. *Geophysical Research Letters*, 43, 2649-2658,
561 doi:10.1002/2016GL067720.

562

563 Fettweis, X., Hanna, E., Lang, C., Belleflamme, A., Erpicum, M., & Gallée, H. (2013). Brief
564 Communication: Important role of the mid-tropospheric atmospheric circulation in the recent
565 surface melt increase over the Greenland ice sheet. *The Cryosphere*, 7, 241-248, doi:10.5194/tc-
566 7-241-2013.

567

568 Fettweis, X., Mabilie, G., Erpicum, M., Nicolay, S., & Van den Broeke, M. (2011). The 1958-
569 2009 Greenland ice sheet surface melt and the mid-tropospheric atmospheric circulation. *Climate
570 Dynamics*, 36, 139-159, doi:10.1007/s00382-010-0772-8.

571

572 Gelaro, R., McCarty, W., Suárez, M.J., Todling, R., Molod, A., Takacs, L., et al. (2017, July 15).
573 The Modern-Era Retrospective Analysis for Research and Applications, Version 2 (MERRA-2).
574 *Journal of Climate*, 30, 5419-5454, doi:10.1175/JCLI-D-16-0758.1.

575

576 Häkkinen, S., Hall, D.K., Shuman, C.A., Worthen, D.L., & DiGirolamo, N.E. (2014). Greenland
577 ice sheet melt from MODIS and associated atmospheric variability. *Geophysical Research*
578 *Letters*, *41*, 1600-1607, doi:10.1002/2013GL059185.

579
580 Hall, D.K., Cullather, R.I., DiGirolamo, N.E., Comiso, J.C., Medley, B.C., & Nowicki, S.M.
581 (2018). A Multilayer Surface Temperature, Surface Albedo, and Water Vapor Product of
582 Greenland from MODIS. *Remote Sensing*, *10*, 555, doi:10.3390/rs10040555.

583
584 Hanna, E., Hall, R.J., Cropper, T.E., Ballinger, T.J., Wake, L., Mote, T., & Cappelen, J. (2018).
585 Greenland blocking index daily series 1851-2015: Analysis of changes in extremes and links
586 with North Atlantic and UK climate variability and change. *International Journal of*
587 *Climatology*, *38*, 3546-3564, doi:10.1002/joc.5516.

588
589 Hanna, E., Cropper, T.E., Hall, R.J., & Cappelen, J. (2016). Greenland Blocking Index 1851-
590 2015: a regional climate change signal. *International Journal of Climatology*, *36*, 4847-4861,
591 doi:10.1002/joc.4673.

592
593 Hanna, E., Fettweis, X., Mernild, S.H., Cappelen, J., Ribergaard, M.H., Shuman, C.A., et al.
594 (2014). Atmospheric and oceanic climate forcing of the exceptional Greenland ice sheet surface
595 melt in summer 2012. *International Journal of Climatology*, *34*, 1022-1037,
596 doi:10.1002/joc.3743.

597

598 Hofer, S., Tedstone, A.J., Fettweis, X., & Bamber, J.L. (2017, June 28). Decreasing cloud cover
599 drives the recent mass loss on the Greenland Ice Sheet. *Science Advances*, 3(6),
600 doi:10.1126/sciadv.1700584.

601
602 Hofer, S., Tedstone, A.J., Fettweis, X., & Bamber, J.L. (2019, July). Cloud microphysics and
603 circulation anomalies control differences in future Greenland melt. *Nature Climate Change*, 9,
604 523-528, <https://doi.org/10.1038/s41558-019-0507-8>.

605
606 Intrieri, J.M., Fairall, C.W., Shupe, M.D., Persson, P.O.G., Andreas, E.L., Guest, P.S., & Moritz,
607 R.E. (2002, September). An annual cycle of Arctic surface cloud forcing at SHEBA. *Journal of*
608 *Geophysical Research*, 107(C10), 8039, doi:10.1029/2000JC000439.

609
610 Johansson, E., Devasthale, A., Tjernström, M., Ekman, A.M.L., & L'Ecuyer, T. (2017).
611 Response of the lower troposphere to moisture intrusions into the Arctic. *Geophysical Research*
612 *Letters*, 44, 2527-2536, doi:10.1002/2017GL072687.

613
614 Lenaerts, J.T.M., Medley, B., van den Broeke, M., & Wouters, B. (2019). Observing and
615 Modeling Ice Sheet Surface Mass Balance. *Reviews of Geophysics*, 57, 376-420,
616 doi:10.1029/2018RG000622.

617
618 Lenaerts, J.T.M., Van Tricht, K., Lhermitte, S., & L'Ecuyer, T.S. (2017). Polar clouds and
619 radiation in satellite observations, reanalyses, and climate models. *Geophysical Research Letters*,
620 44, 3355-3364, doi:10.1002/2016GL072242.

621
622
623
624
625
626
627
628
629
630
631
632
633
634
635
636
637
638
639
640
641
642

Lim, Y-K., Schubert, S.D., Nowicki, S.M.J., Lee, J.N., Molod, A.M., Cullather, R.I., et al. (2016). Atmospheric summer teleconnections and Greenland Ice Sheet surface mass variations: insights from MERRA-2. *Environmental Research Letters*, *11*, doi:10.188/1748-9326/11/2/024002.

Liu, Y., Ackerman, S.A., Maddux, B.C., Key, J.R., & Frey, R.A. (2010, April). Errors in Cloud Detection over the Arctic Using a Satellite Imager and Implications for Observing Feedback Mechanisms. *Journal of Climate*, *23*, 1894-1907, doi:10.1175/2009JCLI3386.1.

Mattingly, K.S., Mote, T.L., & Fettweis, X. (2018). Atmospheric River Impacts on Greenland Ice Sheet Surface Mass Balance. *Journal of Geophysical Research: Atmospheres*, *123*, 8538-8560, doi:10.1029/2018JD028714.

Mattingly, K.S., Ramseyer, C.A., Rosen, J.J., Mote, T.L., & Muthyala, R. (2016). Increasing water vapor transport to the Greenland Ice Sheet revealed using self-organizing maps. *Geophysical Research Letters*, *43*, 9250-9258, doi:10.1002/2016GL070424.

McIlhattan, E.A., L'Ecuyer, T.S., & Miller, N.B. (2017, June). Observational Evidence Linking Arctic Supercooled Liquid Cloud Biases in CESM to Snowfall Processes. *Journal of Climate*, *30*, 4477-4495, doi:10.1175/JCLI-D-16.0666.1.

643 McLeod, J.T., & Mote, T.L. (2016). Linking interannual variability in extreme Greenland
644 blocking episodes to the recent increase in summer melting across the Greenland ice sheet.
645 *International Journal of Climatology*, 36, 1484-1499, doi:10.1002/joc.4440.
646

647 McLeod, J.T., & Mote, T.L. (2015). Assessing the role of precursor cyclones on the formation of
648 extreme Greenland blocking episodes and their impact on summer melting across the Greenland
649 ice sheet. *Journal of Geophysical Research: Atmospheres*, 120, doi:10.1002/2015JD023945.
650

651 Miller, N.B., Shupe, M.D., Cox, C.J., Walden, V.P., Turner, D.D., & Steffen, K. (2015, August
652 1). Cloud Radiative Forcing at Summit, Greenland. *Journal of Climate*, 28, 6267-6280,
653 doi:10.1175/JCLI-D-15-0076.1.
654

655 Mioduszewski, J.R., Rennermalm, A.K., Hammann, A., Tedesco, M., Noble, E.U., Stroeve, J.C.,
656 et al. (2016). Atmospheric drivers of Greenland surface melt revealed by self-organizing maps.
657 *Journal of Geophysical Research: Atmospheres*, 121, doi:10.1002/2015JD024550.
658

659 Neff, W., Compo, G.P., Ralph, F.M., & Shupe, M.D. (2014). Continental heat anomalies and the
660 extreme melting of the Greenland ice surface in 2012 and 1889. *Journal of Geophysical
661 Research: Atmospheres*, 119, 6520-6536, doi:10.1002/2014JD021470.
662

663 Noël, B., van de Berg, W.J., Lhermitte, S., & van den Broeke, M.R. (2019). Rapid ablation zone
664 expansion amplifies north Greenland mass loss, *Science Advances*, 5(9),
665 doi:10.1126/sciadv.aaw0123.

666

667 Nusbaumer, J., Alexander, P.M., LeGrande, A.N., & Tedesco, M. (2019). Spatial shift of
668 Greenland moisture sources related to enhanced Arctic warming. *Geophysical Research Letters*,
669 *46*, 14,723-14,731. <https://doi.org/10.1029/2019GL084633>.

670

671 Papritz, L. & Dunn-Sigouin, E. (2020, September). What Configuration of the Atmospheric
672 Circulation Drives Extreme Net and Total Moisture Transport into the Arctic? *Geophysical*
673 *Research Letters*, *47*, e2020GL089769. <https://doi-org/10.1029/2020GL089769>.

674

675 Pfahl, S., Schwierz, C., Croci-Maspoli, M., Grams, C.M., & Wernli, H. (2015, July 20).
676 Importance of latent heat release in ascending air streams for atmospheric blocking. *Nature*
677 *Geoscience*, *8*, 610-615, doi:10.1038/NGEO2487.

678

679 Platnick, S., Meyer, K.G., King, M.D., Wind, G., Amarasinghe, N., Marchant, B., et al. (2017,
680 January 1). The MODIS Cloud Optical and Microphysical Products: Collection 6 Updates and
681 Examples from Terra and Aqua. *IEEE Transactions on Geoscience and Remote Sensing*, *55*(1),
682 502-525.

683

684 Platnick, S., Li, J.Y., King, M.D., Gerber, H., & Hobbs, P.V. (2001, July 27). A solar reflectance
685 method for retrieving the optical thickness and droplet size of liquid water clouds over snow and
686 ice surfaces. *Journal of Geophysical Research*, *106*(D14), 15,185-15,199.

687

688 Rajewicz, J. & Marshall, S.J. (2014). Variability and trends in anticyclonic circulation over the
689 Greenland ice sheet, 1948-2013. *Geophysical Research Letters*, *41*, 2842-2850,
690 doi:10.1002/2014GL059225.

691

692 Rignot, E., Box, J.E., Burgess, E., & Hanna, E. (2008). Mass balance of the Greenland ice sheet
693 from 1958 to 2007. *Geophysical Research Letters*, *35*(L20502), doi:10.1029/2008GL035417.

694

695 Shepherd, A., Ivins, E.R., Geruo, A., Barletta, V.R., Bentley, M.J., Bettadpur, S.,...Zwally, H.J.
696 (2012, November). A Reconciled Estimate of Ice-Sheet Mass Balance, *Science*, *338*(6111),
697 1183-1189, doi:10.1126/science.1228102.

698

699 Shupe, M.D., Turner, D.D., Walden, V.P., Bennartz, R., Cadeddu, M.P., Castellani, B.B., et al.
700 (2013, February). High and Dry: New Observations of Tropospheric and Cloud Properties above
701 the Greenland Ice Sheet. *Bulletin of the American Meteorological Society*, *94*, 169-186,
702 doi:10.1175/BAMS-D-11-00249.1.

703

704 Shupe, M.D., & Intrieri, J.M. (2004, February). Cloud Radiative Forcing of the Arctic Surface:
705 The Influence of Cloud Properties, Surface Albedo, and Solar Zenith Angle. *Journal of Climate*,
706 *17*, 616-628.

707

708 Tedesco, M., & Fettweis, X. (2020). Unprecedented atmospheric conditions (1948-2019) drive
709 the 2019 exceptional melting season over the Greenland ice sheet. *The Cryosphere*, *14*, 1209-
710 1223. <https://doi:10.5194/tc-14-1209-2020>.

711
712
713
714
715
716
717
718
719
720
721
722
723
724
725
726
727
728
729
730
731
732
733

Tedesco, M., Mote, T., Fettweis, X., Hanna, E., Jeyaratnam, J., Booth, J.F., et al. (2016). Arctic cut-off high drives the poleward shift of a new Greenland melting record. *Nature Communications*, 7(11723), doi:10.1038/ncomms11723.

Tedesco, M., Fettweis, X., van den Broeke, M.R., van de Wal, R.S.W., Smeets, C.J.P.P., van de Berg, W.J., Serreze, M.C., & Box, J.E. (2011). The role of albedo and accumulation in the 2010 melting record in Greenland. *Environmental Research Letters*, 6, doi:10.1088/1748-9326/6/1/014005.

Välisuo, I., Vihma, T., Pirazzini, R., & Schäfer, M. (2018). Interannual Variability of Atmospheric Conditions and Surface Melt in Greenland in 2000-2014. *Journal of Geophysical Research: Atmospheres*, 123, 10,443-10,463, <https://doi.org/10.1029/2018JD028445>.

van As, D., Hubbard, A.L., Hasholt, B., Mikkelsen, A.B., van den Broeke, M.R., & Fausto, R.S. (2012). Large surface meltwater discharge from Kangerlussuaq sector of the Greenland ice sheet during the record-warm year 2010 explained by detailed energy balance observations. *The Cryosphere*, 6, 199-209, doi:10.5194/tc-6-199-2012.

van den Broeke, M., Box, J., Fettweis, X., Hanna, E., Noël, B., Tedesco, M., ...van Kampenhout, L. (2017). Greenland Ice Sheet Surface Mass Loss: Recent Developments in Observation and Modeling. *Current Climate Change Report*, 3, 345-356, doi:10.1007/s40641-017-0084-8.

734 van den Broeke, M., Smeets, P., & Ettema, J. (2009). Surface layer climate and turbulent
735 exchange in the ablation zone of the west Greenland ice sheet. *International Journal of*
736 *Climatology*, 29, 2309-2323, doi:10.1002/joc.1815.

737

738 van den Broeke, M., Smeets, P., Ettema, J., van der Veen, C., van de Wal, R., & Oerlemans, J.
739 (2008). Partitioning of melt energy and meltwater fluxes in the ablation zone of the west
740 Greenland ice sheet. *The Cryosphere*, 2, 179-189.

741

742 Van Tricht, K., Lhermitte, S., Lenaerts, J.T.M., Gorodetskaya, I.V., L'Ecuyer, T.S., Noël, B., et
743 al. (2016). Clouds enhance Greenland ice sheet meltwater runoff. *Nature Communications*,
744 7(10266), doi:10.1038/ncomms10266.

745

746 Wang, W., Zender, C.S., van As, D., & Miller, N.B. (2019, January). Spatial Distribution of Melt
747 Season Cloud Radiative Effects Over Greenland: Evaluating Satellite Observations, Reanalyses,
748 and Model Simulations Against In Situ Measurements. *Journal of Geophysical Research:*
749 *Atmospheres*, 124, 57-71. <https://doi.org/10.1029/2018JD028919>.

750

751 Wills, R.C.J., White, R.H., & Levine, X.J. (2019, November). Northern Hemisphere Stationary
752 Waves in a Changing Climate. *Current Climate Change Reports*, 5, 372-389.
753 <https://doi.org/10.1007/s40641019-00147-6>.

754

755 Woods, C., Caballero, R., & Svensson, G. (2013). Large-scale circulation associated with
756 moisture intrusions into the Arctic during winter. *Geophysical Research Letters*, *40*, 4717-4721,
757 doi:10.1002/grl.50912.

758

759 Woollings, T., Barriopedro, D., Methven, J., Son, S-W., Martius, O., Harvey, B., ... Seneviratne,
760 S. (2018). Blocking and its Response to Climate Change. *Current Climate Change Reports*, *4*,
761 287-300. <https://doi.org/10.1007/s40641-018-0108-z>.

762

763 Yang, W., Guo, X., Yao, T., Yang, K., Zhao, L., Li, S., & Zhu, M. (2011). Summertime surface
764 energy budget and ablation modeling in the ablation zone of a maritime Tibetan glacier. *Journal*
765 *of Geophysical Research*, *16*(D14116), doi:10.1029/2010JD015183.

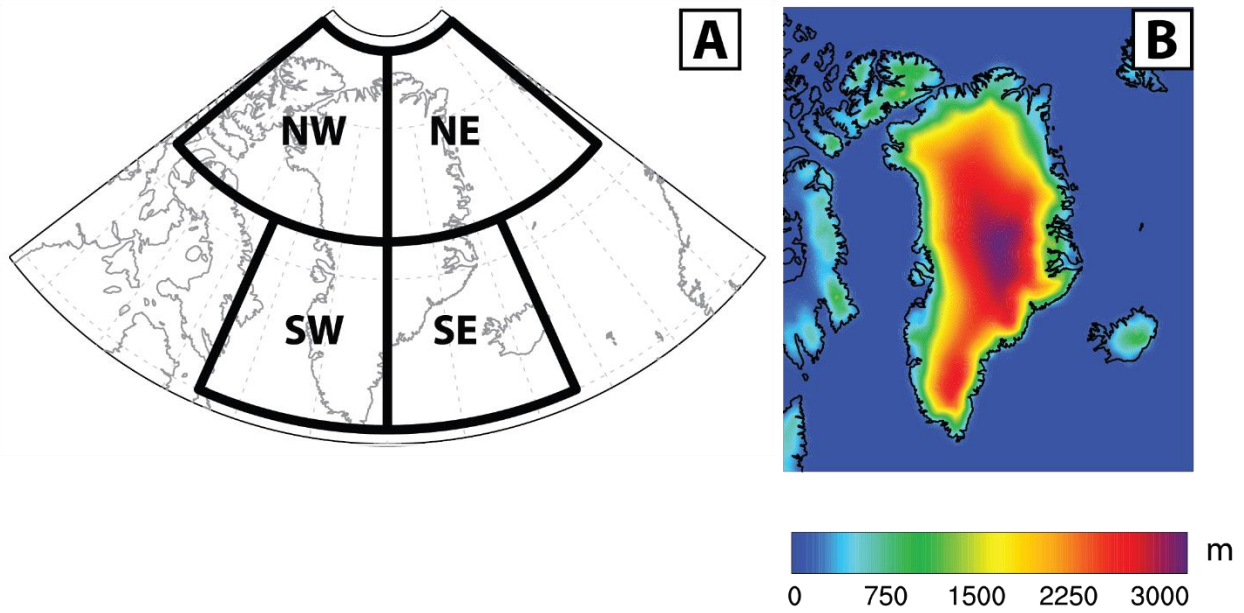
766 Tables

767 Table 1: D-S algorithm original and modified parameters

Threshold	Units	Original D-S	Modified D-S
Duration (D)	Days	5	4
Amplitude (A)	Unitless	1.5	1.2
Spatial Scale (S)	km^2	2.5×10^6	1.0×10^6
Overlap (O)	Percentage	50	50

768

Author Manuscript



770

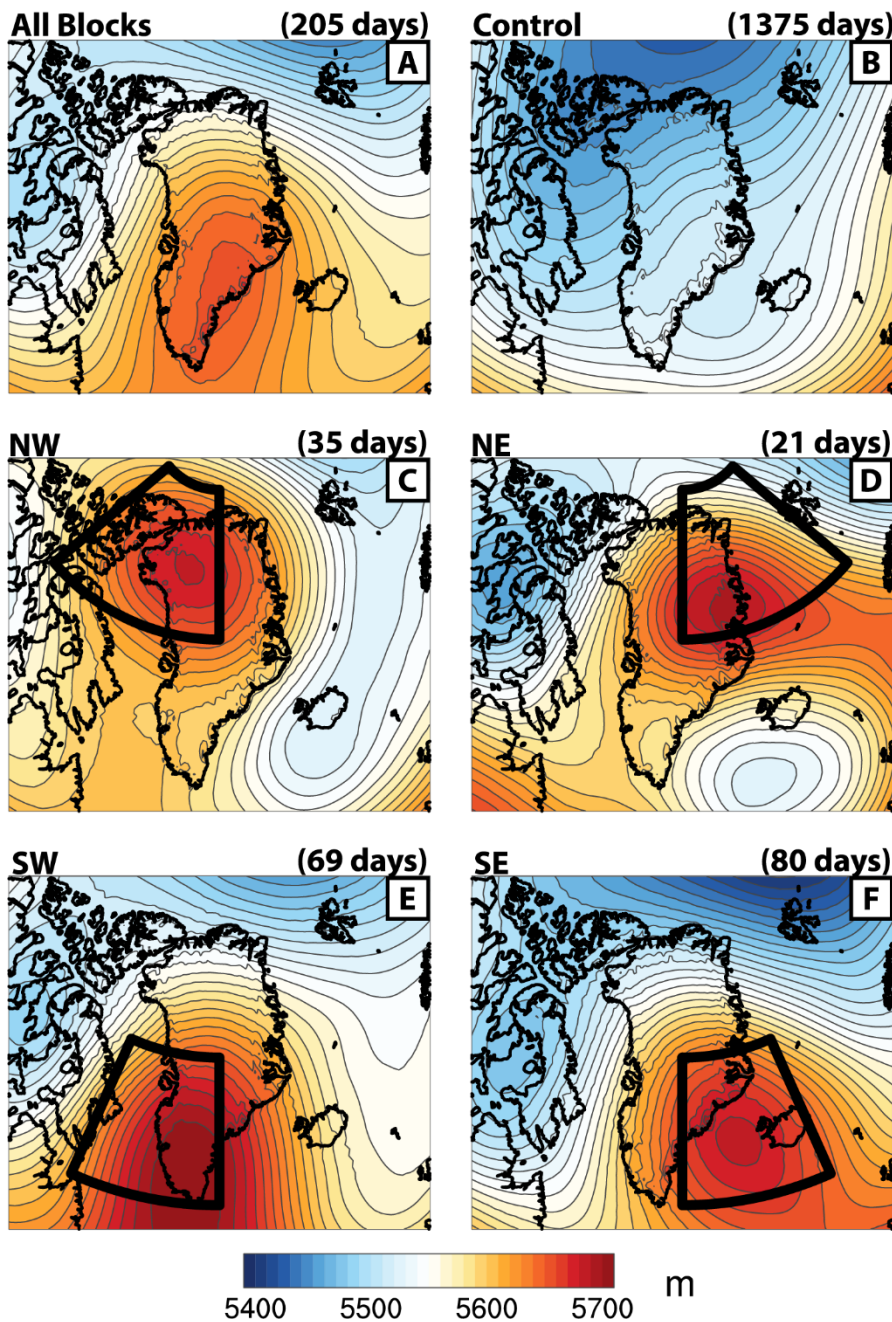
771 Fig. 1: A) Equal-area Greenland block quadrants. The quadrants are Northwest (NW), Northeast

772 (NE), Southwest (SW), and Southeast (SE). B) Present-day topography of the GrIS derived from

773 MERRA-2 surface geopotential data.

774

Average 500hPa Geopotential Height (m) for Block and Control Days



775

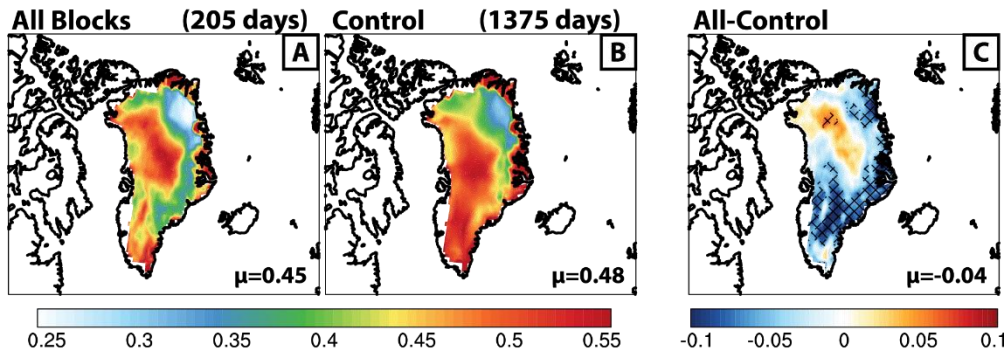
776

777

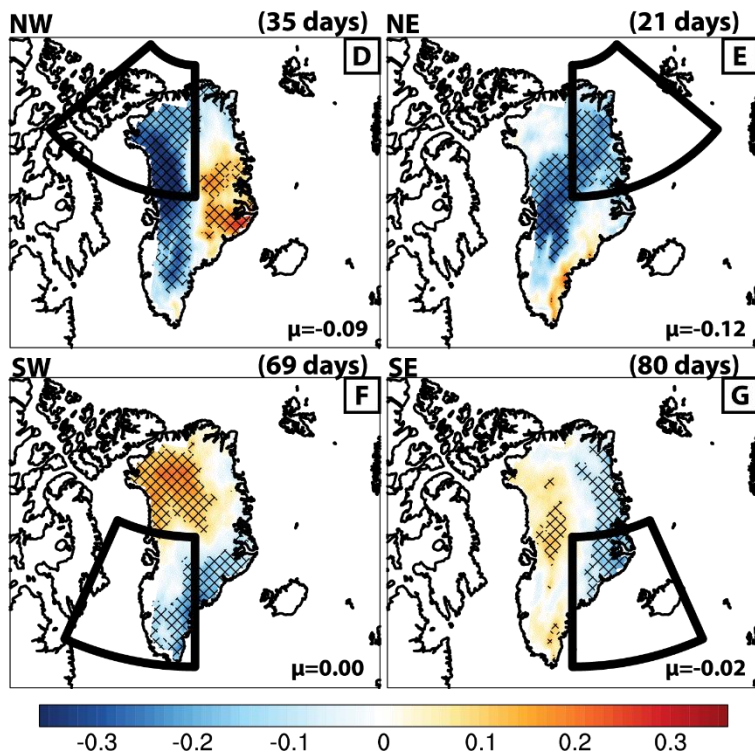
778

Fig. 2: Composite 500hPa geopotential height plots for A) “All Blocks”, B) “Control”, C) NW, D) NE, E) SW, and F) SE block days. Day counts are listed above each panel. Black boxes in C-F represent the corresponding block quadrant boundaries.

Cloud Fraction for Block and Control Days



Differences by Block Quadrant (Block-Control)



779

780

781

782

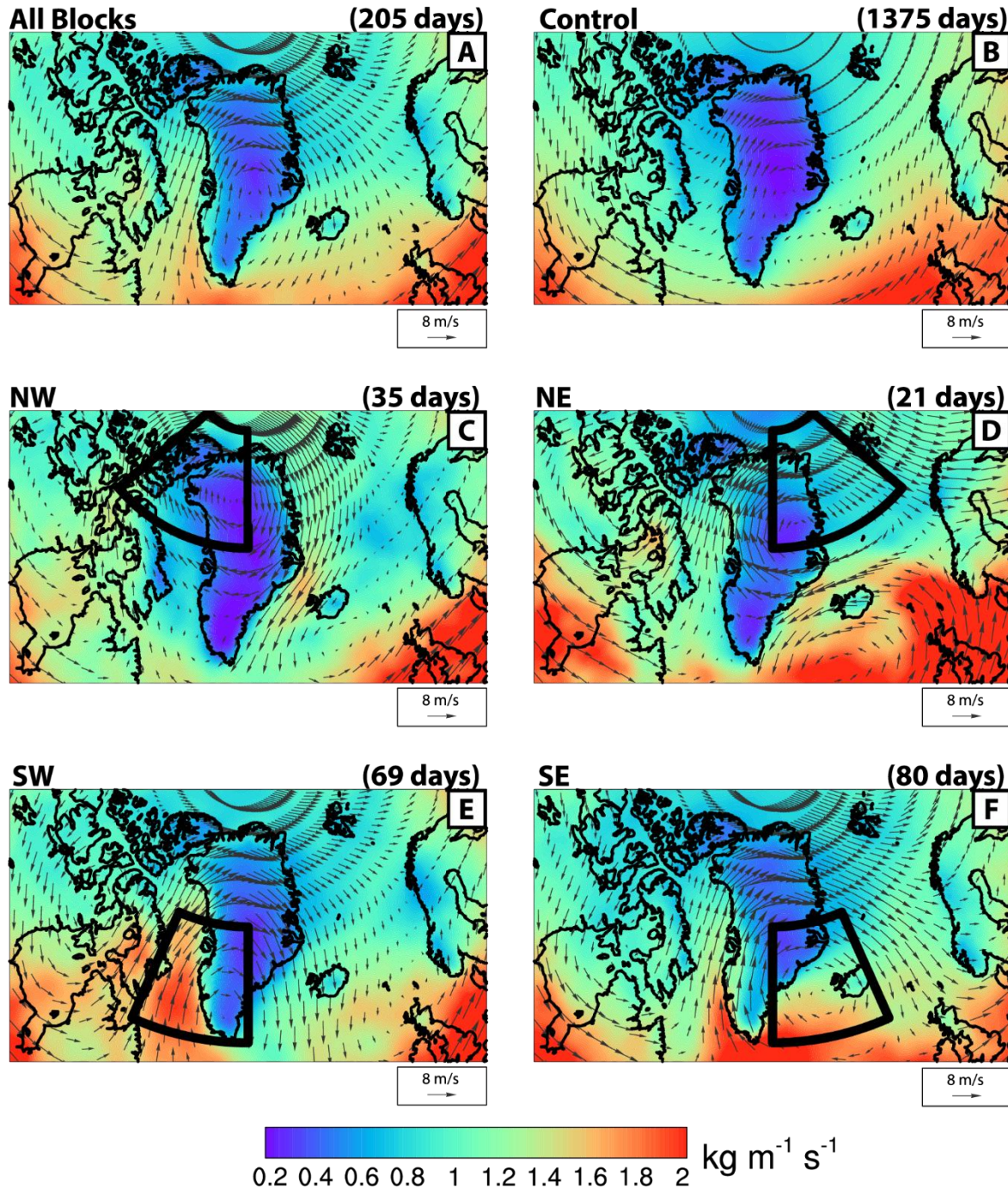
783

784

785

Fig. 3: MOD06 cloud fraction. Panels A and B show absolute cloud fraction for “All Blocks” and “Control”, respectively, and their difference is in panel C. Quadrant-based cloud fraction changes with respect to “Control” are in panels D through G, with GrIS averages (μ) in the lower right-hand corner of each panel. The black boxes are the corresponding quadrant boundaries. Cross-hatching in panels C through G represents statistically significant differences (95% confidence level).

Integrated Moisture Transport ($\text{kg m}^{-1} \text{s}^{-1}$) and Winds (m/s) for Block and Control Days



787

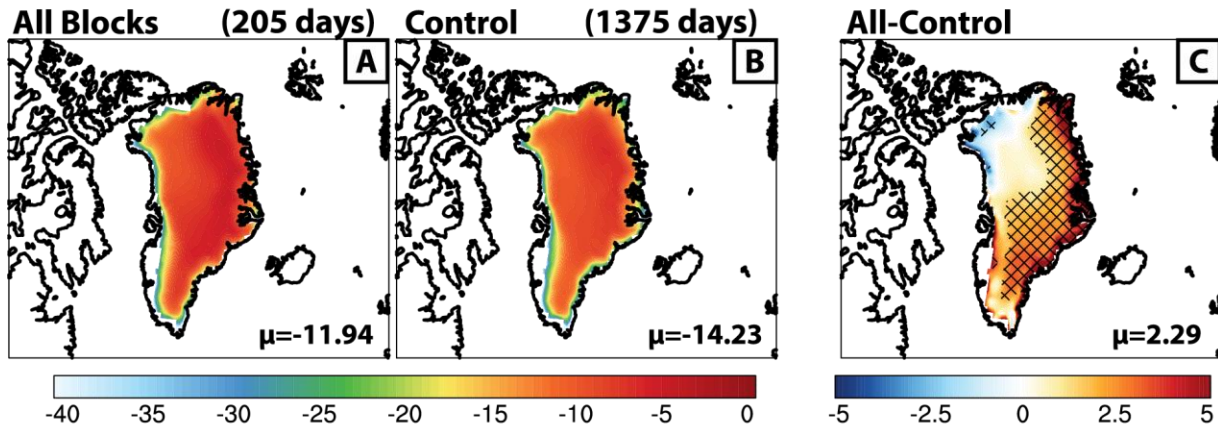
788

Fig. 4: Pressure weighted vertically integrated moisture transport (shading) and winds (\vec{W} ;

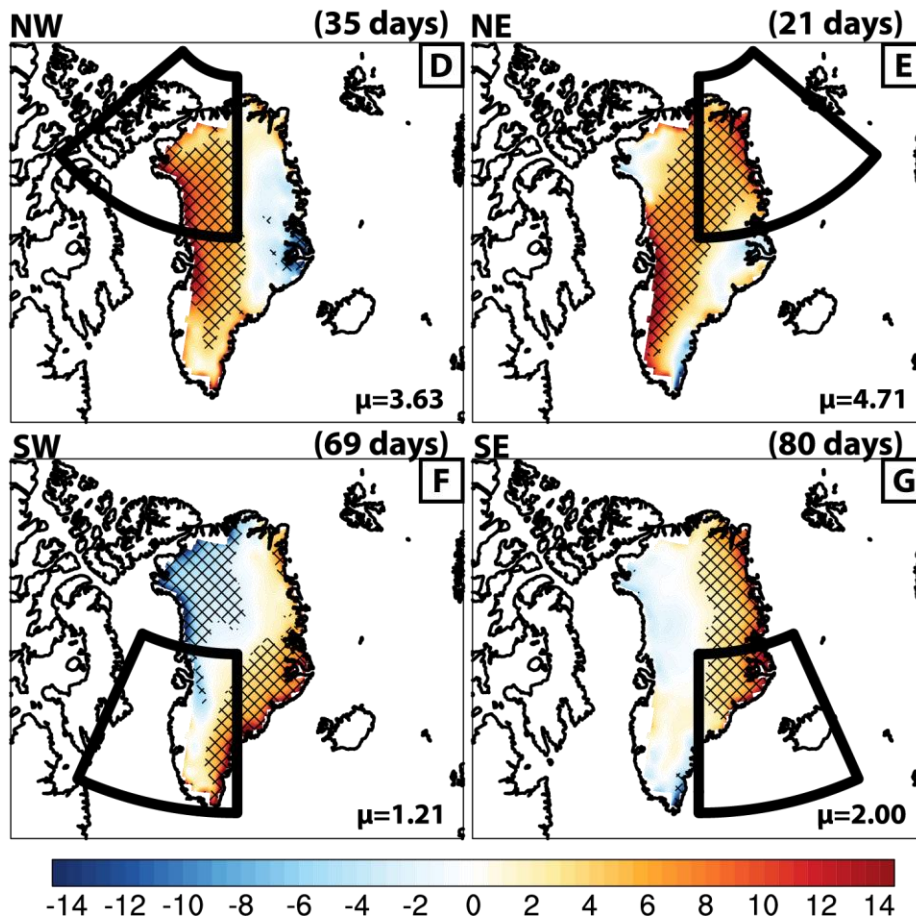
789

arrows). The reference wind speed and arrow size are shown below each panel.

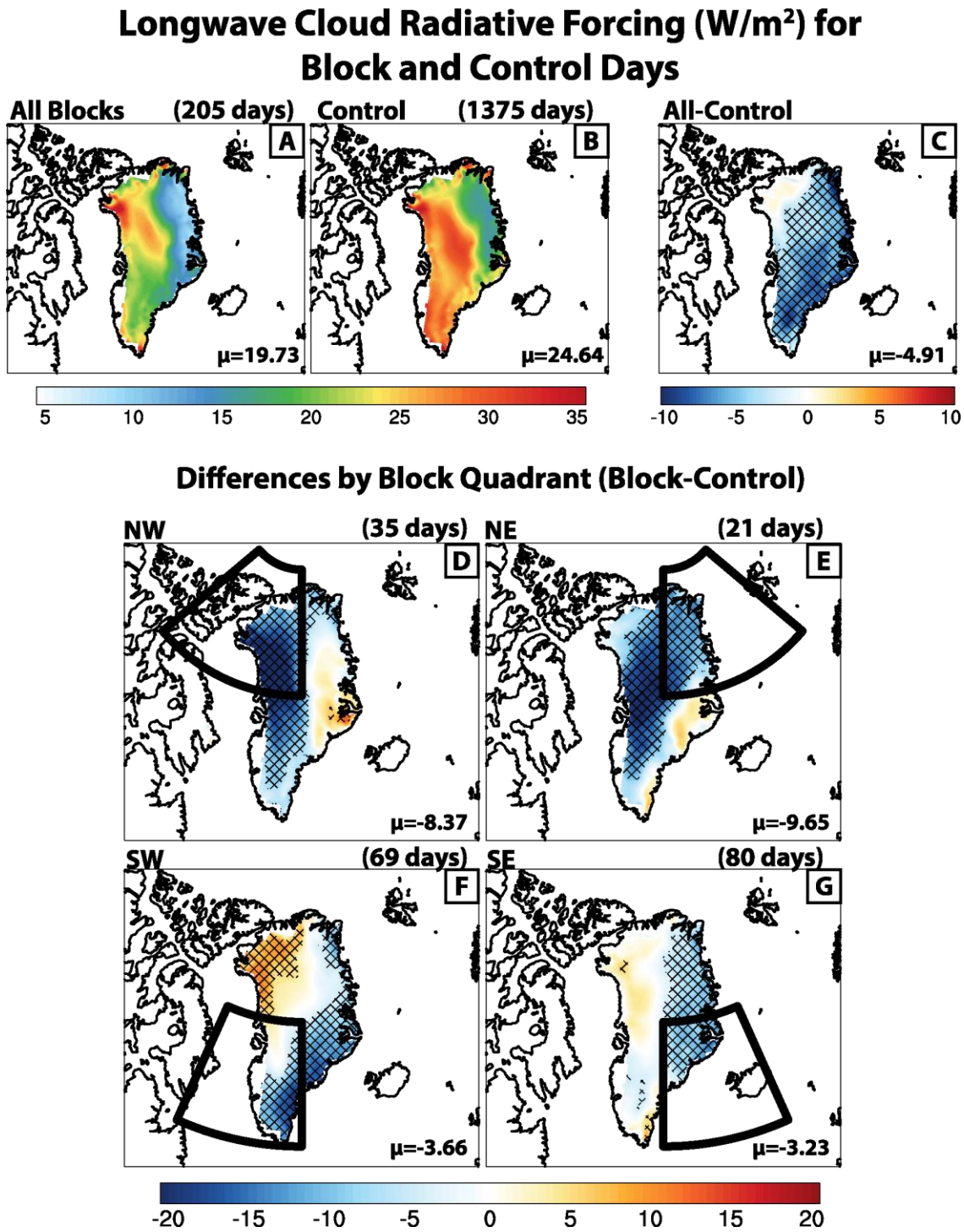
Shortwave Cloud Radiative Forcing (W/m^2) for Block and Control Days



Differences by Block Quadrant (Block-Control)



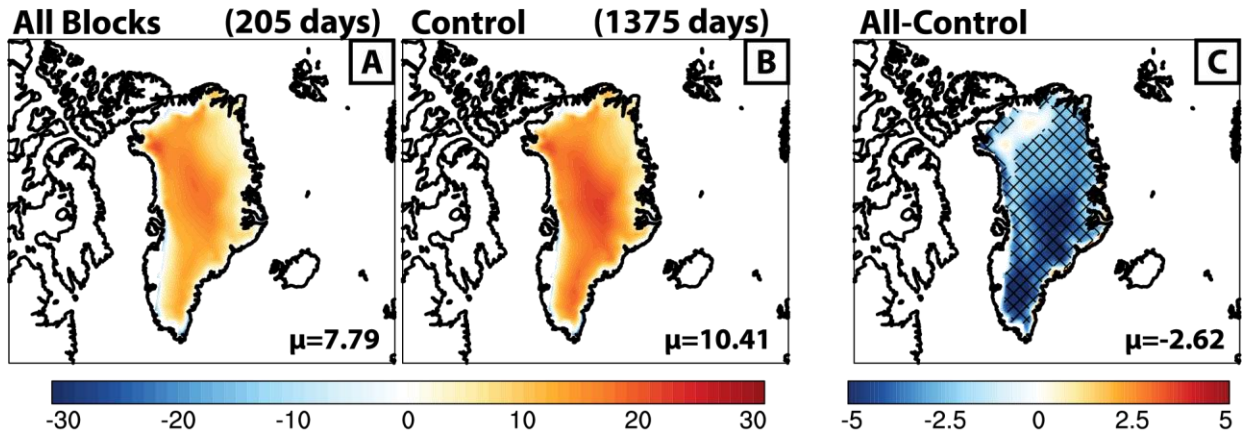
792 Fig. 5: Same as Fig. 3, but for MERRA-2 derived surface net shortwave cloud radiative forcing
793 at the surface (W/m^2).



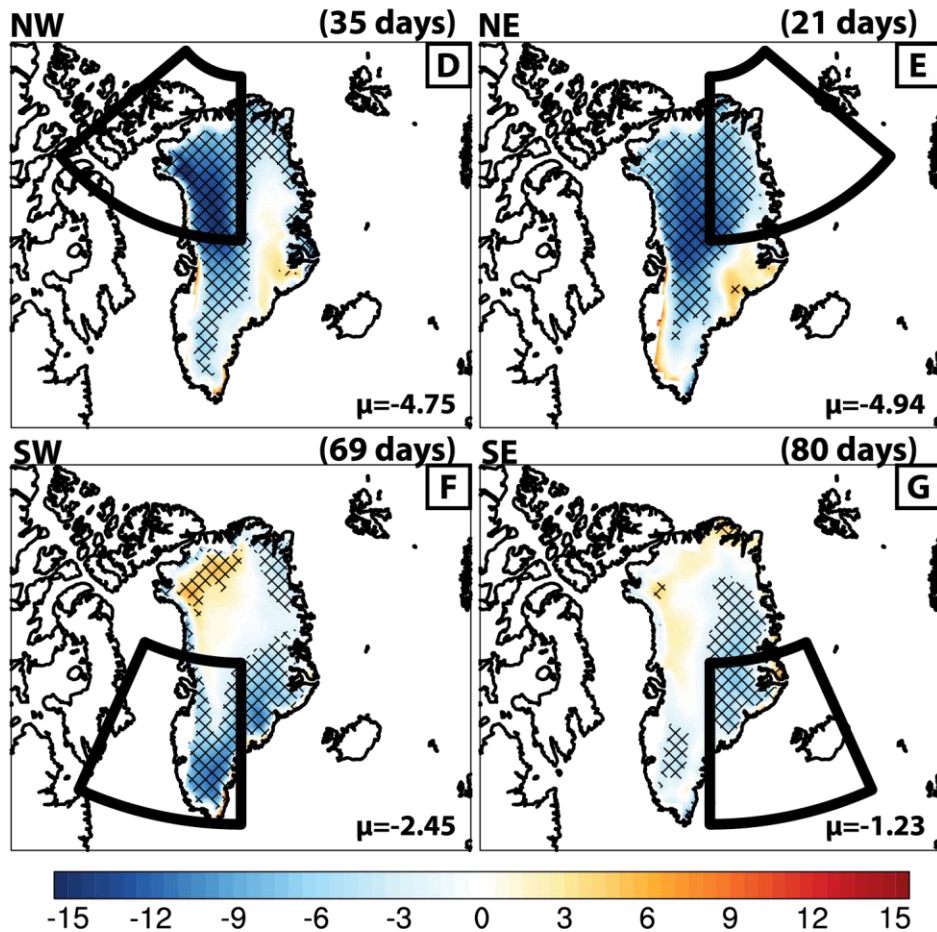
794

795 Fig. 6: Same as Fig. 3, but for MERRA-2 derived surface net longwave cloud radiative forcing at
796 the surface (W/m^2).

Total Cloud Radiative Forcing (W/m^2) for Block and Control Days



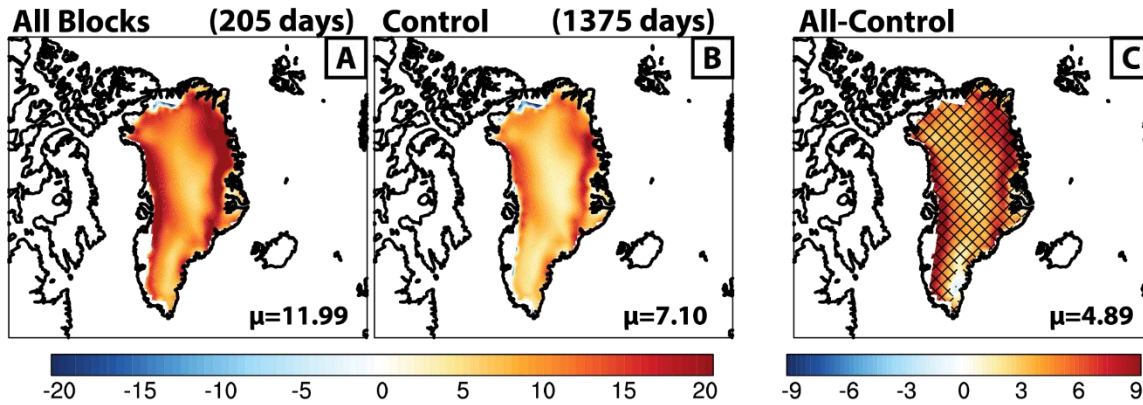
Differences by Block Quadrant (Block-Control)



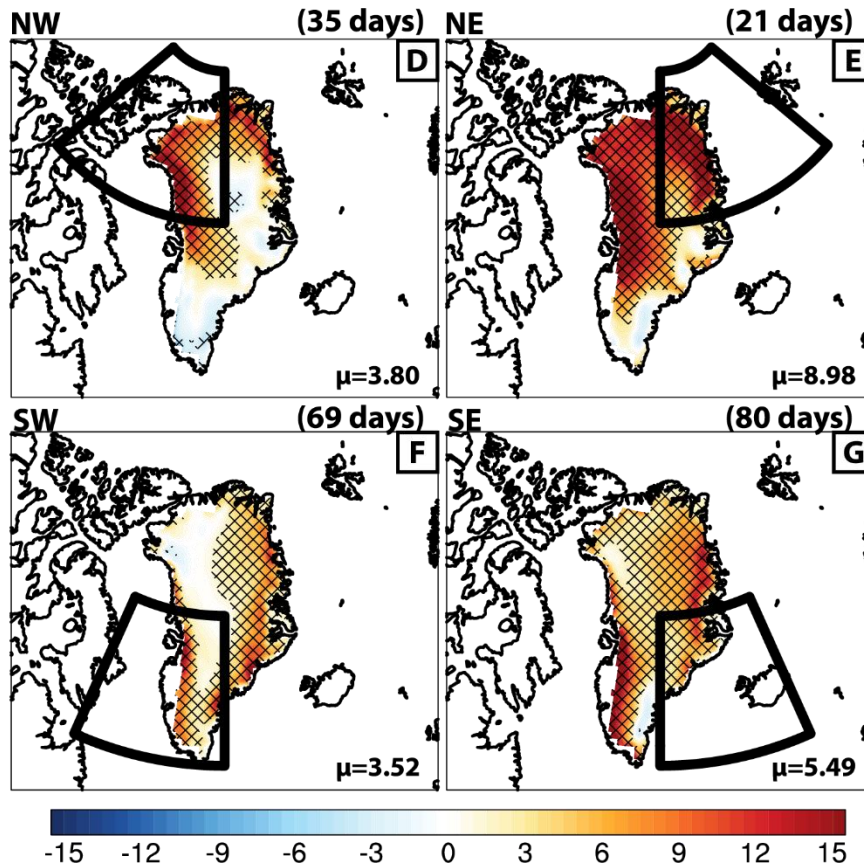
798

799 Fig. 7: Same as Fig. 3, but for MERRA-2 derived total surface cloud radiative forcing.

Sensible Heat Flux (W/m^2) for Block and Control Days



Differences by Block Quadrant (Block-Control)



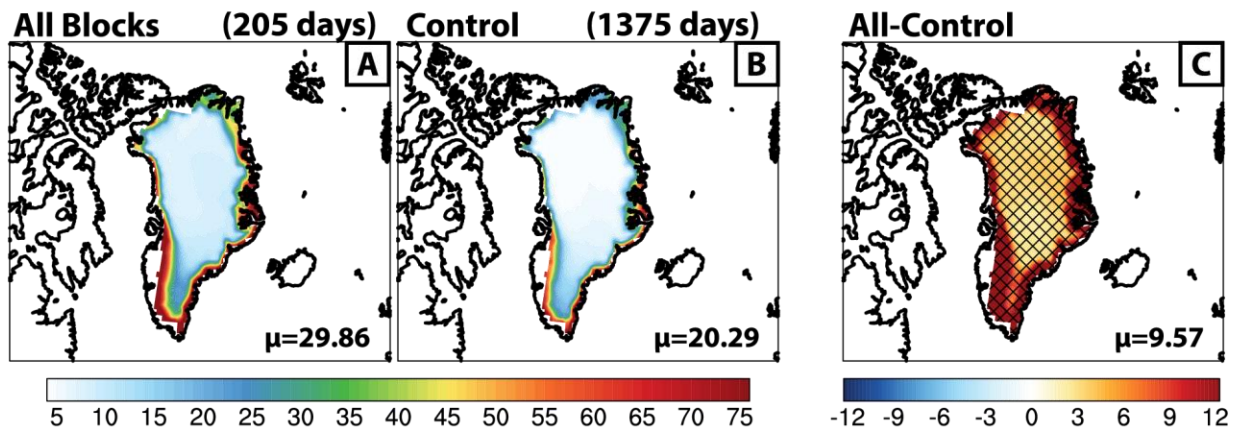
801

802 Fig. 8: Same as Fig. 3, but for MERRA-2 sensible heat flux. Positive quantities are directed into

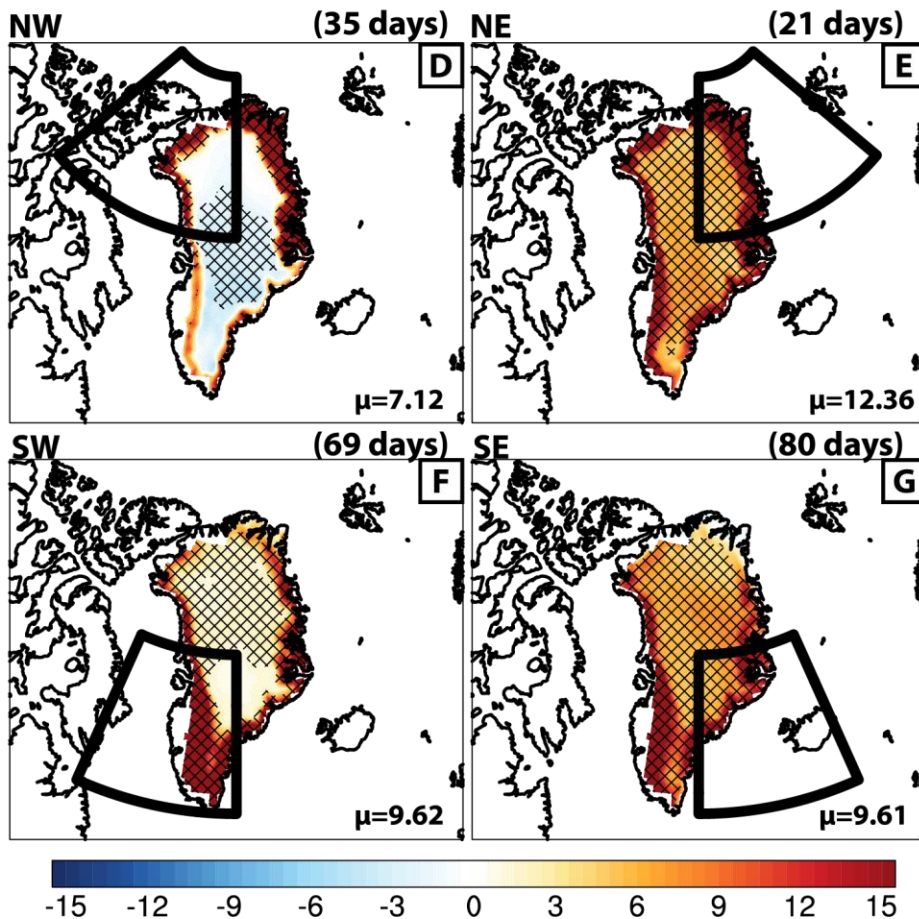
803 the surface.

804

Total Surface Energy Flux (W/m^2) for Block and Control Days



Differences by Block Quadrant (Block-Control)

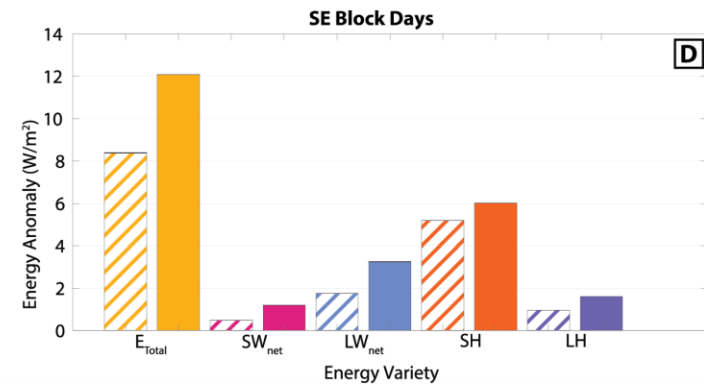
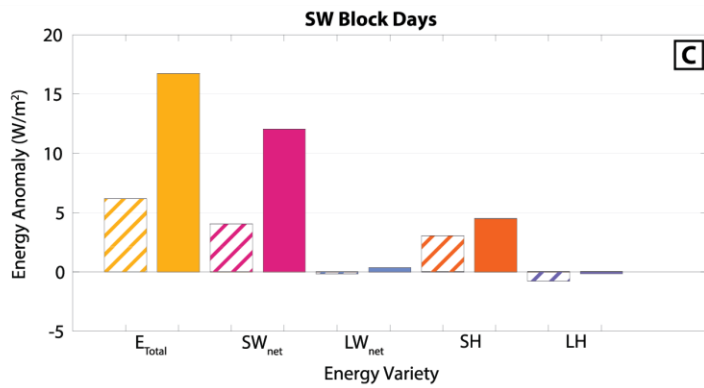
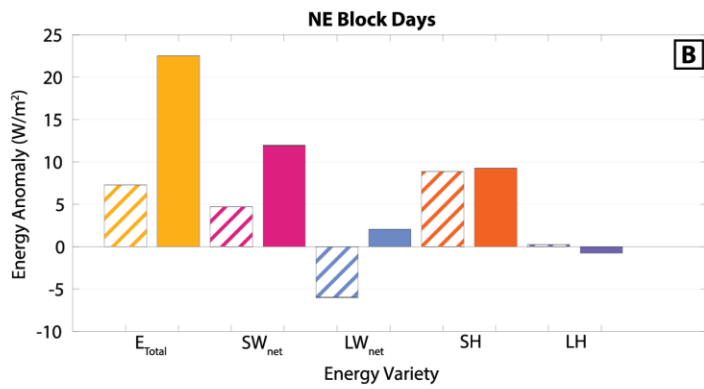
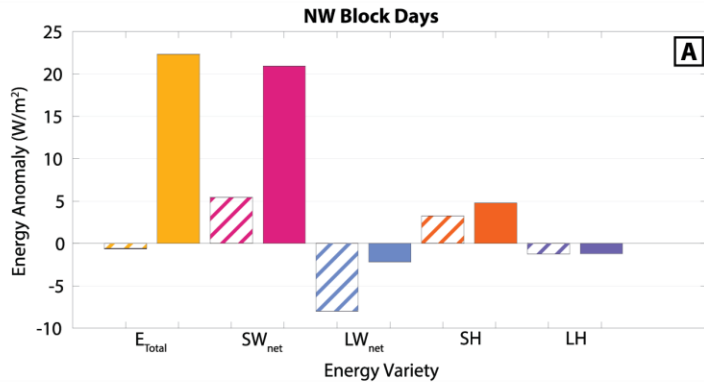


805

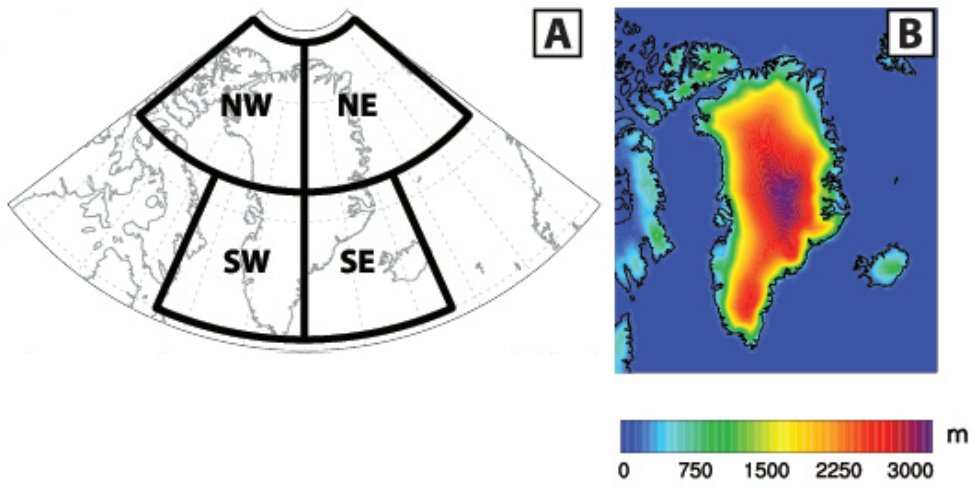
806 Fig. 9: Same as Fig. 3, but for MERRA-2 derived total surface energy flux.

807

Greenland-Average Accumulation and Ablation Zone Energy Anomalies for each Block Location

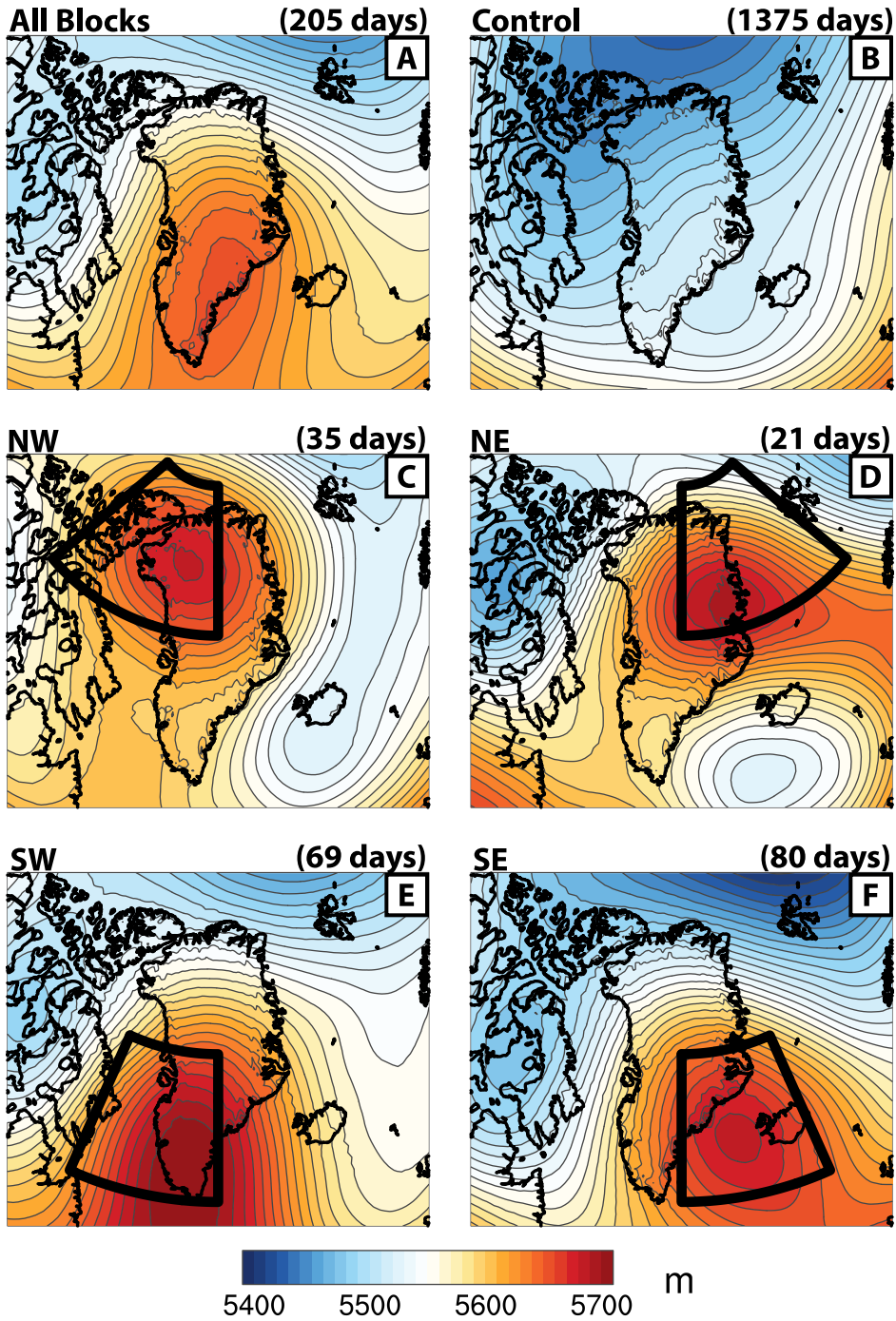


809 Fig. 10: Spatially-averaged total surface energy flux, net shortwave, net longwave, sensible heat,
810 and latent heat anomalies separated into accumulation zone (cross-hatched bars, elevations above
811 1500m (e.g., van den Broeke et al., 2008)) and ablation zone (elevations below 1500m) for A)
812 NW block days, B) NE block days, C) SW block days, and D) SE block days.

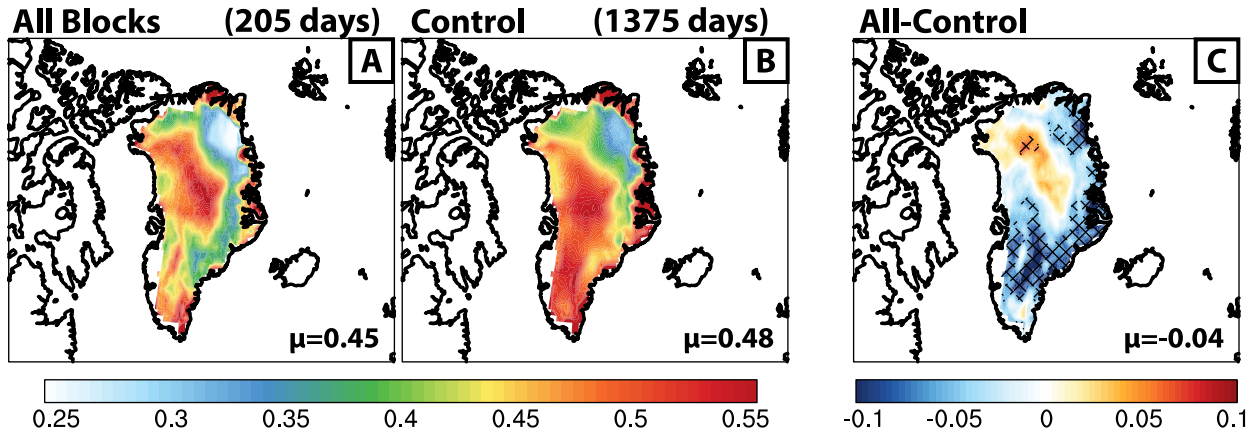


JGRD_56603_2020JD033172-f01-z-.jpg

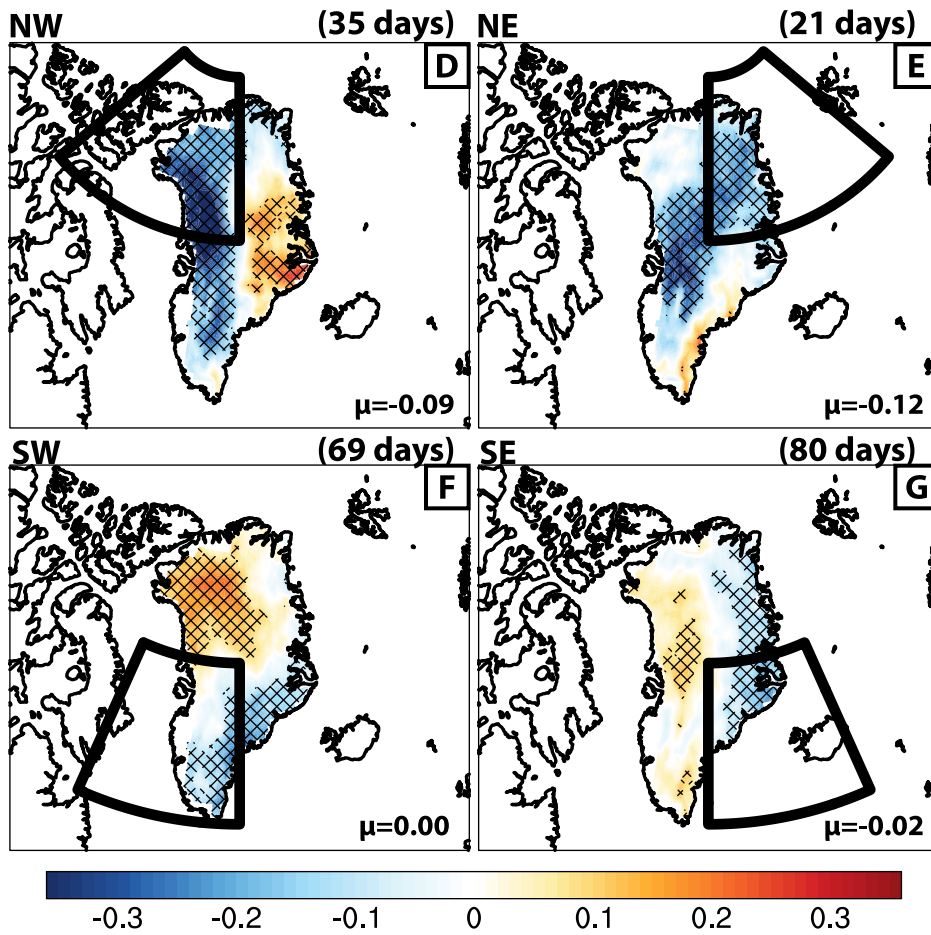
Average 500hPa Geopotential Height (m) for Block and Control Days



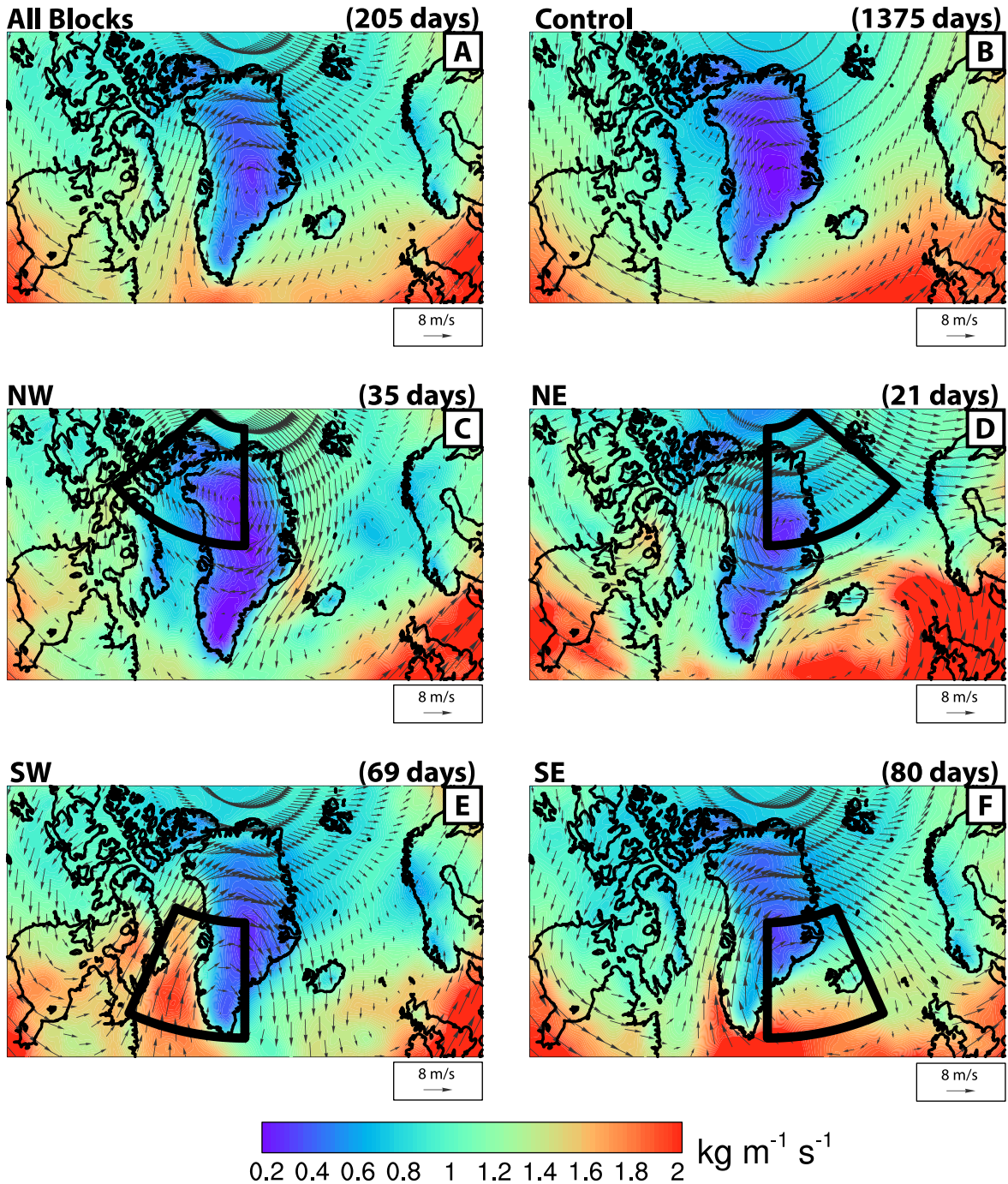
Cloud Fraction for Block and Control Days



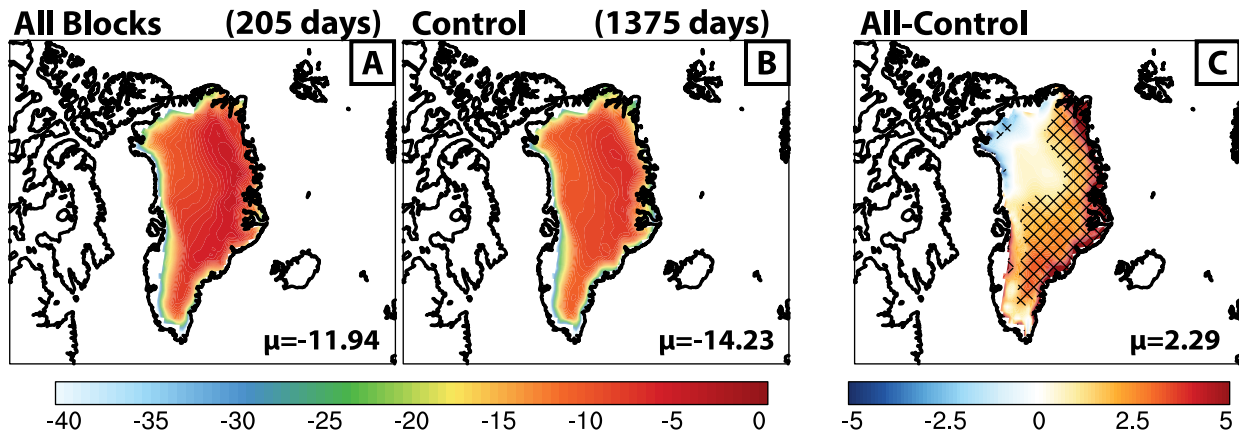
Differences by Block Quadrant (Block-Control)



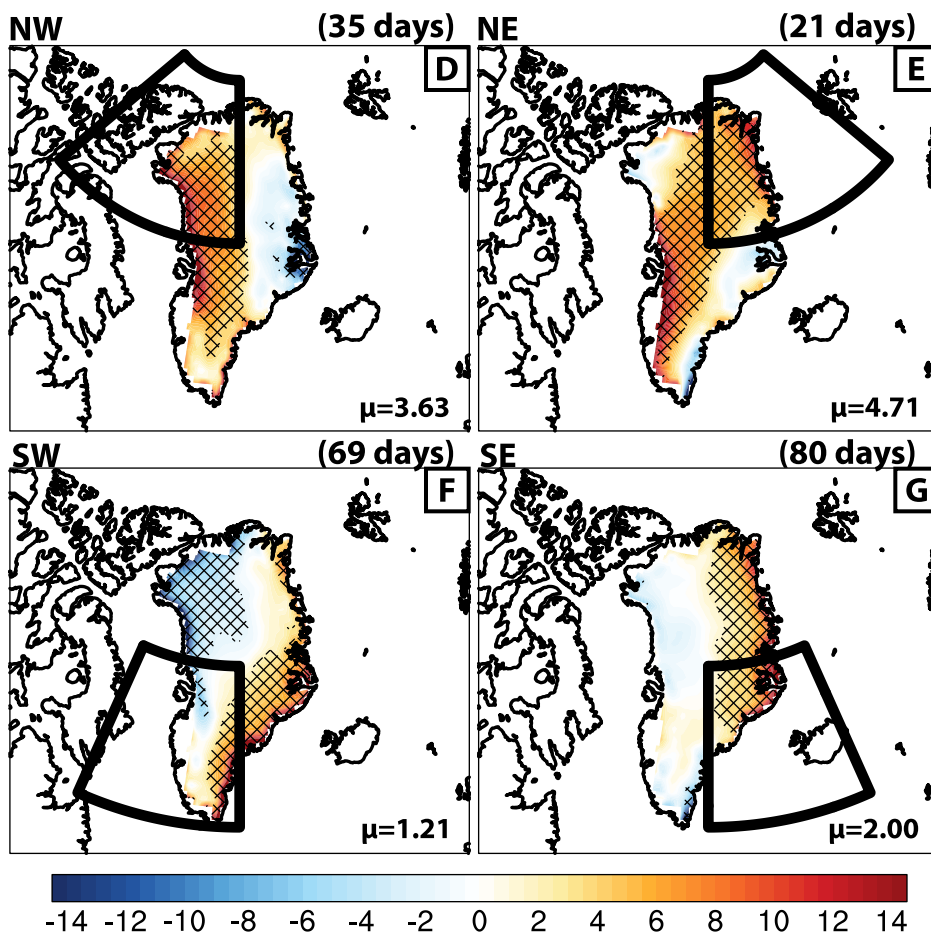
Integrated Moisture Transport ($\text{kg m}^{-1} \text{s}^{-1}$) and Winds (m/s) for Block and Control Days



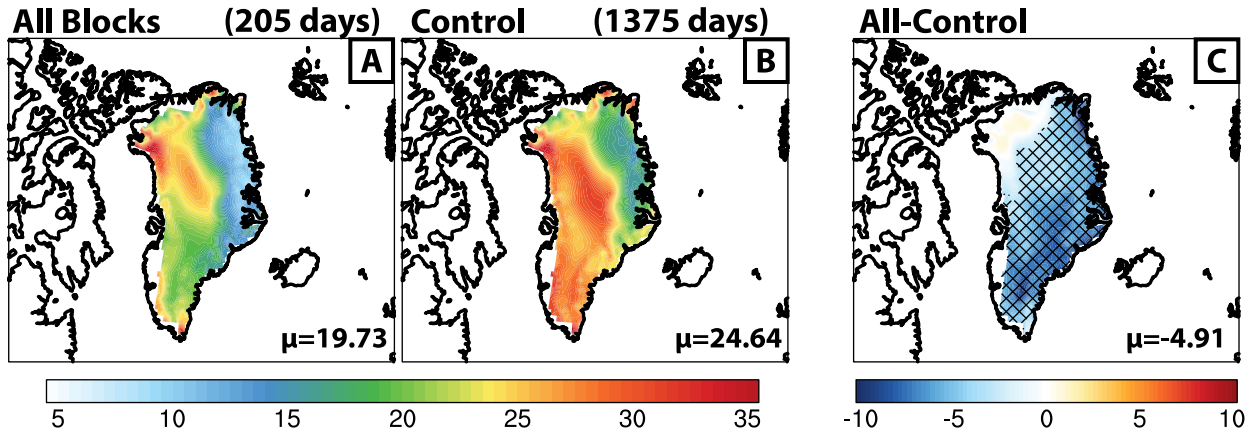
Shortwave Cloud Radiative Forcing (W/m^2) for Block and Control Days



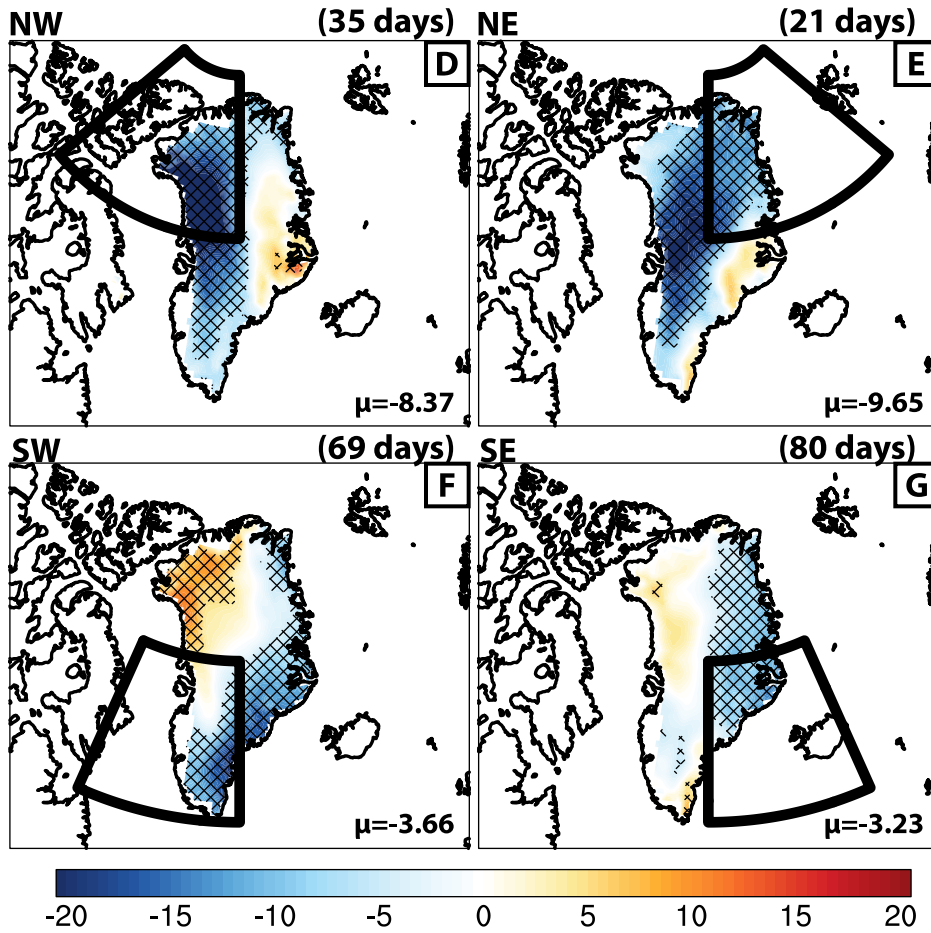
Differences by Block Quadrant (Block-Control)



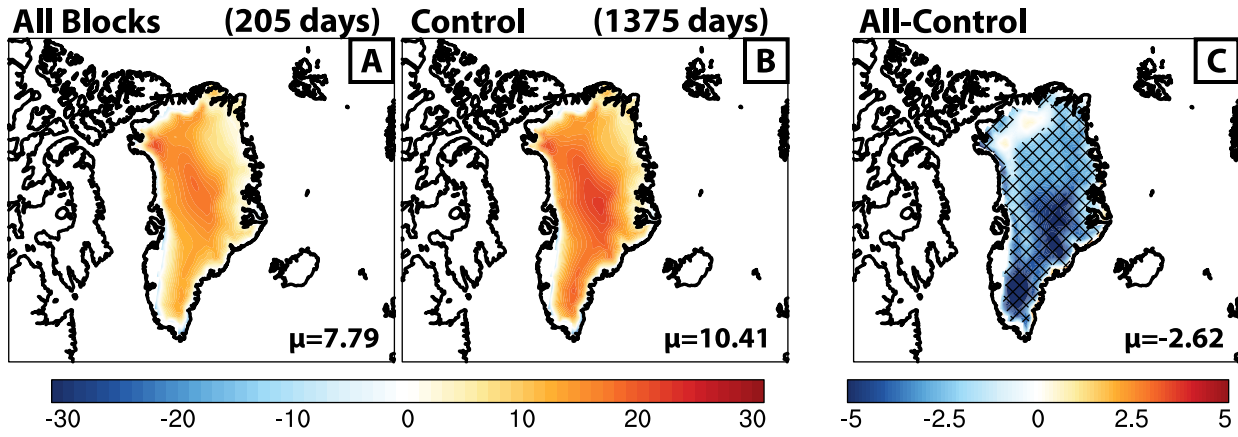
Longwave Cloud Radiative Forcing (W/m^2) for Block and Control Days



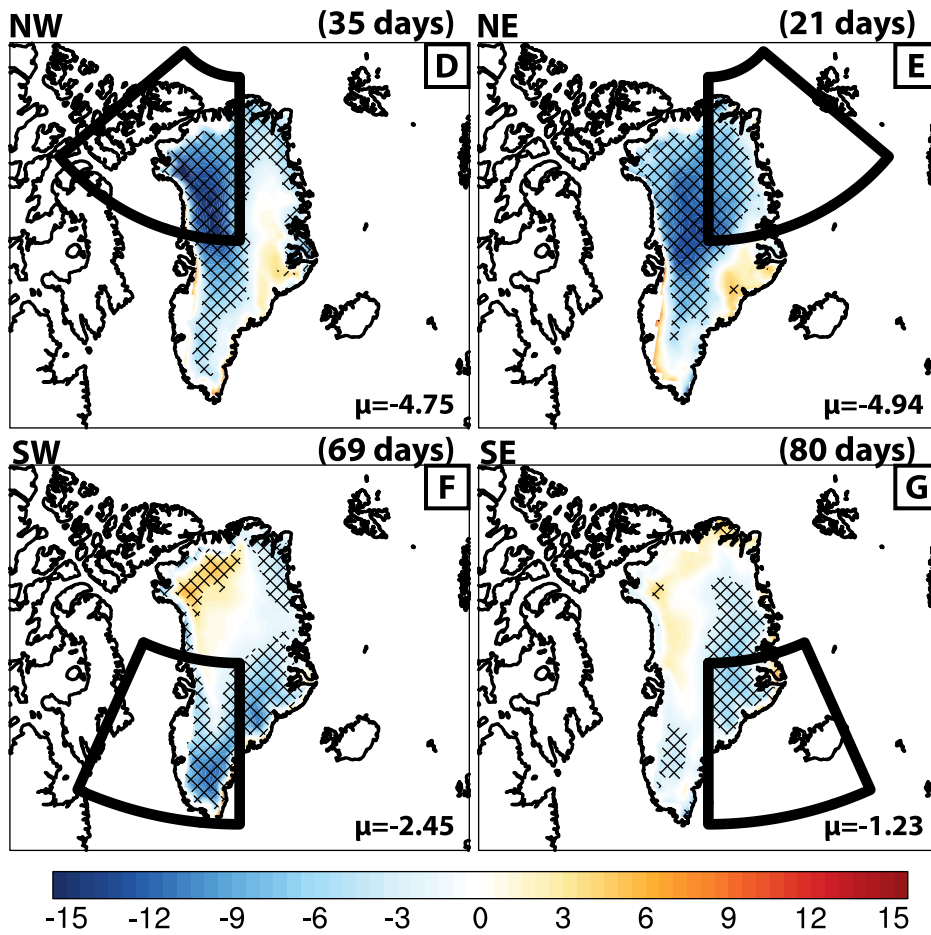
Differences by Block Quadrant (Block-Control)



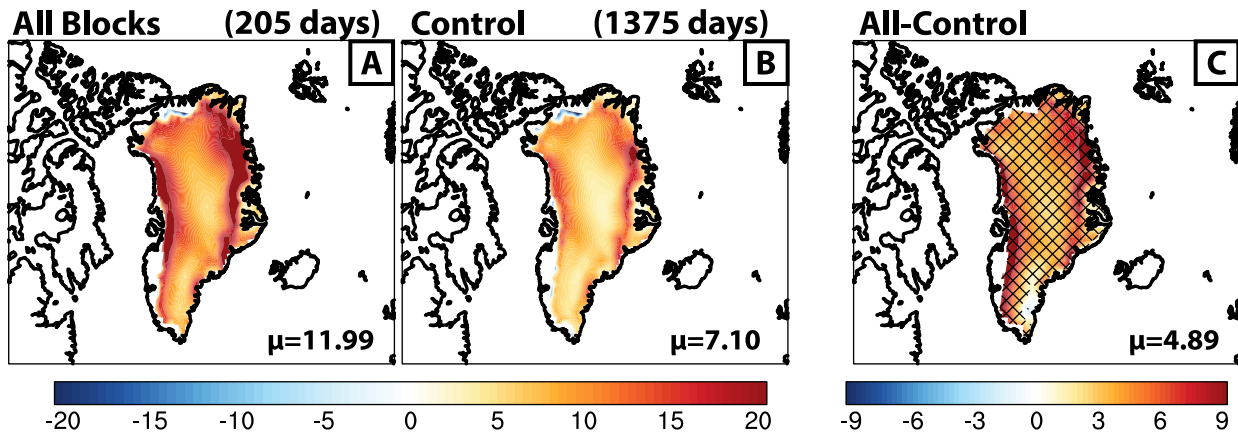
Total Cloud Radiative Forcing (W/m^2) for Block and Control Days



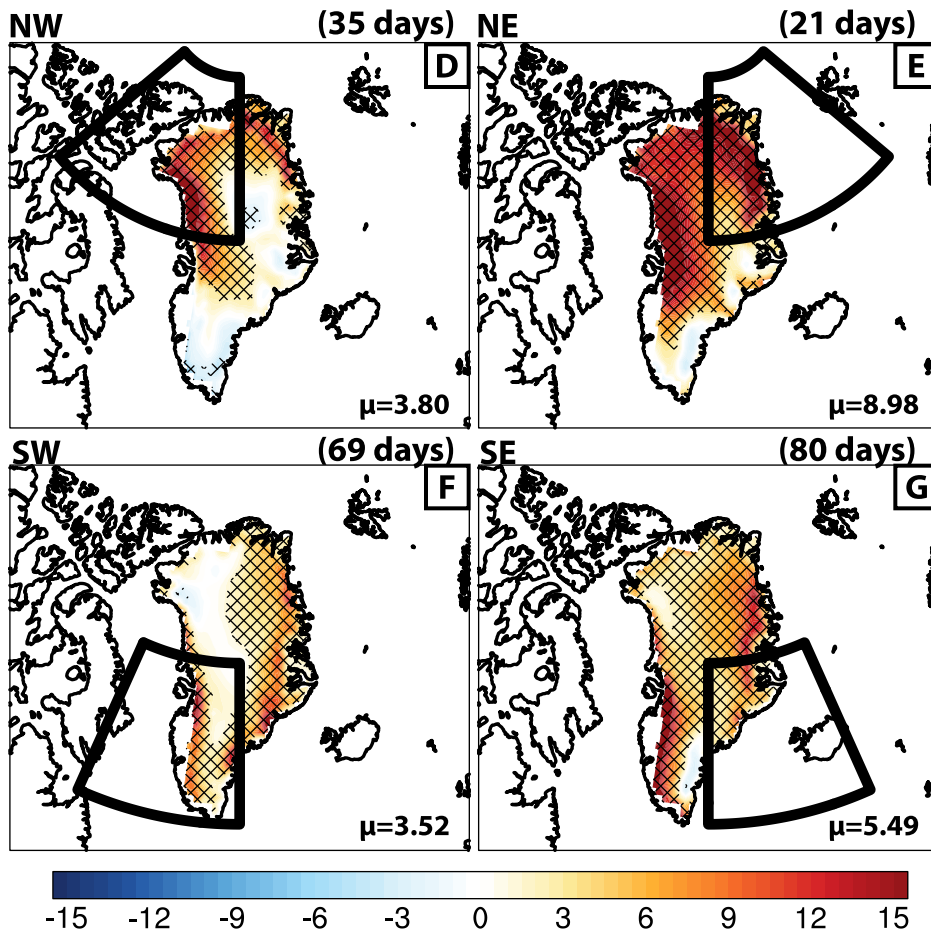
Differences by Block Quadrant (Block-Control)



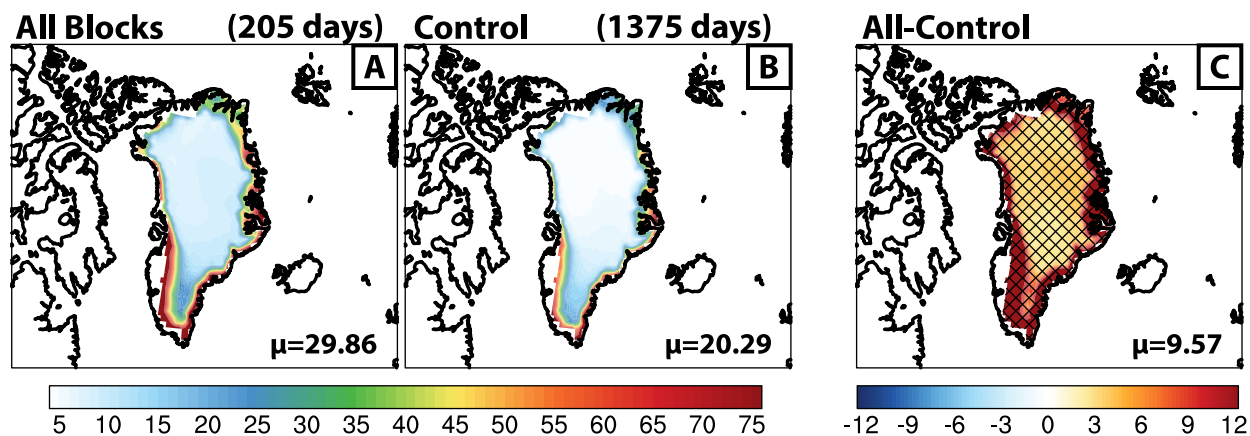
Sensible Heat Flux (W/m^2) for Block and Control Days



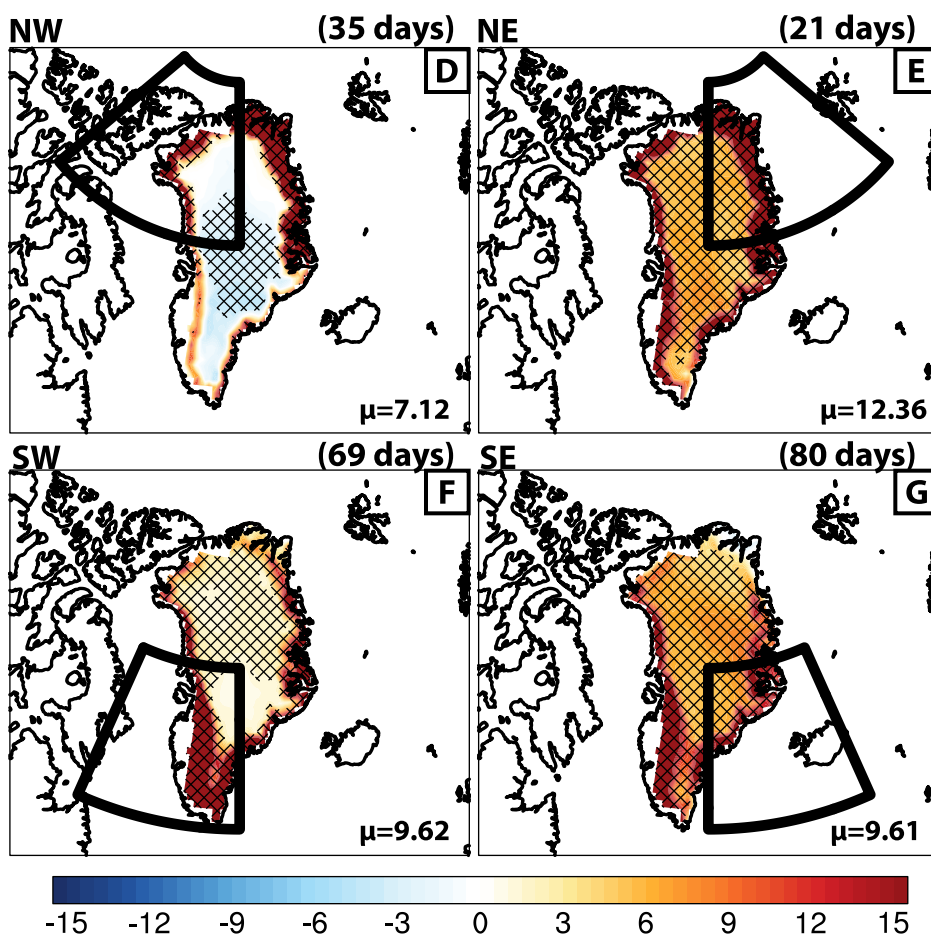
Differences by Block Quadrant (Block-Control)



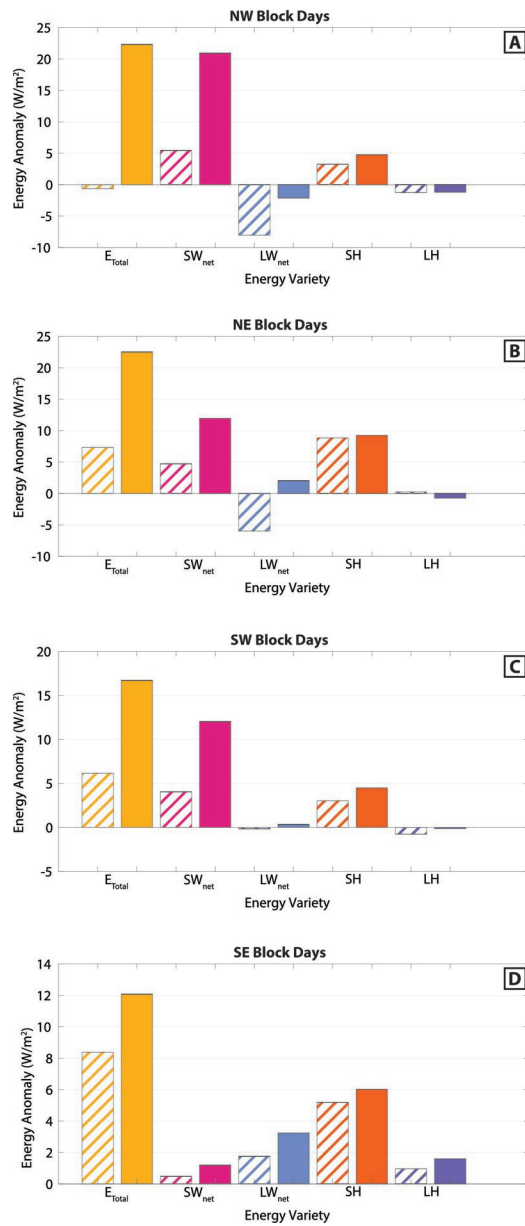
Total Surface Energy Flux (W/m^2) for Block and Control Days



Differences by Block Quadrant (Block-Control)



Greenland-Average Accumulation and Ablation Zone Energy Anomalies for each Block Location



jgrd_56603_2020jd033172-f10-z-.eps